DEVELOPING ACTIVITY DATA FROM REMOTE SENSING FOR REDD+ MONITORING IN TROPICAL MIOMBO WOODLANDS

By

Daniel J. Zelenak

A THESIS

Submitted to
Michigan State University
in partial fulfillment of the requirements
for the degree of

Forestry—Master of Science

2018

ABSTRACT

DEVELOPING ACTIVITY DATA FROM REMOTE SENSING FOR REDD+ MONITORING IN TROPICAL MIOMBO WOODLANDS

By

Daniel J. Zelenak

The country of Malawi is experiencing some of the highest rates of deforestation in Africa. Of particular concern are the country's Miombo woodlands—a unique type of dry woodland that is made up from a mosaic of upper and lower canopy species. Miombo woodlands are threatened by expanding agriculture and demand for fuel wood, which is the primary energy source for the majority of Malawi's population. Efforts to map areas of Miombo degradation can be assisted by remote sensing technologies and data sets, which can be much more cost efficient than in-situ measurements. An effort was made to map the locations of deforestation and degradation of Malawi's Miombo woodlands by comparing time-series Landsat data. NDVI and fractional cover were used to quantify the presence of vegetation throughout time, and a change algorithm is used to identify areas of vegetation loss. This information can be used to develop activity data which guides REDD+ efforts in the country of Malawi.

This thesis is dedicated to my family. Thank you for your unwavering support.

ACKNOWLEDGEMENTS

The work of this thesis was made possible by funding from the Malawi PERFORM project and also by support from the Global Observatory for Ecosystem Services Lab at Michigan State University's Department of Forestry.

TABLE OF CONTENTS

LIST OF TABLES

LIST OF FIGURES

KEY TO ABBREVIATIONS

6S: Second Simulation of the Satellite Signal in the Solar Spectrum

AFOLU: Agriculture, Forestry and Other Land Use

AOT: Aerosol Optical Thickness

AVHRR: Advanced Very High Resolution Radiometer

DN: Digital Number

DOS: Dark Object Subtraction

DOY: Day of Year

EROS: Earth Resources Observation and Science Center

ETM+: Enhanced Thematic Mapper Plus

FOLU: Forestry and Other Land Use

*f*C: Fractional Cover

GHG: Greenhouse Gas

GLOVIS: Global Visualization Tool

$GtCO_2eq/yr$: Gigatons of Carbon Dioxide Equivalents per Year

Ha: Hectare

IPCC: Intergovernmental Panel on Climate Change

LUC: Land-use Change

LULCC: Land-use and Land Cover Change

LiDAR: Light Detection and Ranging

MODIS: Moderate Resolution Imaging Spectroradiometer

MSAVI-2: Modified Soil Adjusted Vegetation Index 2

NDVI: Normalized Difference Vegetation Index

NIR: Near Infrared

OLI: Operational Land Imager

PERFORM: Protecting Ecosystems and Restoring Forests in Malawi

SWIR: Short-wave Infrared

TM: Thematic Mapper

TOA: Top of Atmosphere

UNFAO: Food and Agriculture Organization of the United Nations

USGS: United States Geological Survey

WRS-2: World Reference System 2

Chapter 1: Introduction

I. Remote Sensing of Forests and Woodlands

Remote sensing is the science of collecting observational data on a phenomena using an instrument which is not in direct contact with the phenomena being observed. Since the early 1970s remote sensing has been used to map and monitor the earth's surface, and considerable emphasis has been focused on monitoring the land surface. Such instruments have been deployed in aircraft or on earth orbiting satellites and have used active and passive sources of energy for detection and measurement of surface properties. Some forms of active remote sensing include RADAR and SONAR, in which the instrument provides the source of energy that is being emitted to interact with a target surface and measured as a reflected signal. Passive remote sensing refers to instruments that use a natural source of energy to collect information about a target. For example, a satellite that measures the radiant energy from solar output reflected from the earth surface is considered a passive instrument; such instruments measure the interactions of the sun's energy with the surface of the earth. The radiant energy, or electromagnetic energy, that strikes the earth is absorbed or reflected by different surface objects to varying degrees according a specific spectral response of the surface material, allowing measurements of the surface properties across different parts of the electromagnetic spectrum. This allows materials to be identified based on their unique spectral signatures (Lillesand, Kiefer, and Chipman 2008). One of the most important earth observations is that of land used and land cover change (LULCC) monitoring using optical sensors on polar orbiting satellites, such as the Landsat series which has been continuously operating through a series of platforms since 1973.

The use of remote sensing to identify different types of land use and land-cover as well as monitor change has been well established as a body of theory and application in the remote sensing technical communities. One of the great advantages of routine repeat observations from orbital systems is the ability to consistently monitor change by comparing imagery throughout time for the same areas of the earth. As such satellite remote sensing has also been demonstrated as an effective means for determining the extent of deforestation and forest degradation, which are forms of LULCC (Goetz and Dubaya 2011; Skole and Tucker 1993). Forests are of particular interest in the field of LULCC because they play a significant role in many important environmental processes and problems, such as the global carbon cycle (Bonan 2008), surface-climate interactions, quantification of richness of biodiversity, and information on human systems including livelihoods and food security (UNFAO 2010).

Much work has been done using satellite data for measuring forest cover and forest cover loss in the tropics (Broich, et al. 2011; Broich, et al. 2011; Hansen, et al. 2008; Hansen, Stehman, et al. 2008; Hansen et al. 2003; Hansen, et al. 2010; Hansen et al. 2009; Navratil 2013; Skole and Tucker 1993; Matricardi et al. 2007; Matricardi et al. 2010). The abundance of research focused on tropical deforestation shows how important the tropical forest ecosystems are to the rest of the biosphere, and it also highlights how serious the problem of forest loss is in these regions.

Although far less studied than closed canopy tropical forests, LULCC in tropical woodlands and savannas around the world is also an important agent of the global environment. There is particular concern for the woodlands of Africa, especially the Miombo woodlands and the rich biodiversity that they contain. These ecosystems cover approximately 2.7 million km^2 and constitute the largest area of tropical seasonal woodlands globally (Frost 1996). However, as elsewhere (e.g. South America), much of the remote sensing monitoring work in Africa has focused on tropical rainforests (e.g. Matthew C. Hansen, Roy, et al. 2008). Miombo woodlands have not been studied as extensively with remote sensing, but some country-specific work has been done to examine the potential conversion land supporting Miombo.

The woodlands referred to as Miombo are a mosaic of over 8,500 different species. The most prevalent canopy species are from the family Fabaceae, subfamily Caesalpinioideae, and include the genera *Brachystegia*, *Julbernardia*, and *Isoberlinia*. While Miombo can occur as a closed-canopy woodland, most places in which it occurs are open canopy systems with an abundance of under-canopy flora that thrive due to the ability of sunlight to pass through the upper canopy layer. The geographic distribution of Miombo in Africa includes the region north of the Equator extending south of the Tropic of Capricorn. This includes Tanzania, the Democratic Republic of the Congo, Angola, Zambia, Malawi, Zimbabwe, and Mozambique. A distinction can be made between wet and dry Miombo, which is based upon the amount of rainfall that a particular region receives. However, all Miombo is characterized by a warm seasonal wet season (Frost 1996; Ribeiro et al. 2012; Desanker et al. 1997).

Miombo experiences seasonal variation which makes certain times of the year more ideal for remote sensing observations. There are 5 distinguishable phenology periods: a warm and dry pre-rain season in September and October, an early rainy season in November and December, a mid-rainy season in January and February, a late rainy season in March and April, and a cool early dry season from May to August. The majority of Miombo species lose their leaves in the dry season from August to October. New leaves begin forming in the warm and dry period before the rainy season begins (Chidumayo and Frost 1996). An ideal time to use remote sensing for monitoring Miombo is during the early dry season before significant leaf-loss has begun (Hudak and Wessman 2000). Furthermore, the minimum canopy cover for a land area to be defined as a forest is 10% and must cover a minimum of 0.5 hectares according to a definition used by the United Nations Food and Agriculture Organization (UNFAO 2015). Using leaf-on imagery makes it possible to detect forest cover at the Landsat resolution of 30-meters.

II. Climate Change, REDD+, and Malawi

Human activities, such as the burning of fossil fuels, cause the release of carbon dioxide (CO_2) to the atmosphere. CO_2 is one of the gaseous forms that carbon takes in the global carbon cycle. The global carbon cycle includes processes that cycle carbon between biological and geochemical forms: carbon enters the biosphere via primary production (i.e. photosynthesis) and is transferred to the hydrosphere and atmosphere via chemical reactions or physical processes. Respiration returns carbon to the atmosphere. Removals from the atmosphere to the oceans occur through both biological production and physical-chemical diffusion. The oceans return carbon to the atmosphere through biological and physical-chemical process. CO_2 is a GHG because its molecular structure readily absorbs radiation and radiates heat energy to the earth's surface that would otherwise escape into space. This is the greenhouse effect, which as a naturally occurring process is important because this trapped heat allows the earth to be warm enough to support life. CO_2 is just one of several radiatively-active gasses (e.g. chlorofluorocarbons, methane (CH_4) and nitrous oxide (N_2O)) that are released by human activities. CO_2 is an important GHG when discussing the human role in climate change because it is capable of remaining in the atmosphere for long periods of time, which allows for a net accumulation if total emissions of CO_2 are greater than sinks over time. Studies have shown that the burning of fossil fuels has caused a steady and quantifiable increase in the concentration of atmospheric CO_2 since the industrial revolution (Keeling et al. 1976; IPCC 1990); from 1750 to 2011 there was approximately 2,040

$GtCO_2$ in emissions, of which 40% still remains in the atmosphere (IPCC 2014a). GHGs are known to be responsible for the majority of the observed increase in global average surface temperatures by 0.5°C from 1951 to 2010. (IPCC 2014a; IPCC 2014b).

Deforestation and forest degradation are significant contributors to the total amount of anthropogenic GHG emissions. These forms of LULCC represent emissions of CO_2 because they diminish or entirely remove the capacity of the land to assimilate carbon from the atmosphere via primary production, and they reduce the overall stock of carbon stored on land. When stocks of carbon in ecosystems are reduced by deforestation and degradation, carbon in transferred to the atmosphere through biological decomposition or rapid oxidation (e.g. fires). Regeneration of ecosystems provide removals of carbon from the atmosphere when stocks of carbon increase. Coupled with increasing amounts of CO_2 emissions from burning fossil fuels, these forms of LULCC represent a net flux of CO_2 to the atmosphere. Globally the Agriculture, Forestry, and Other Land Use (AFOLU) sector contributed approximately 10-12 $GtCO_2eq$/yr (Gigatons of CO_2 equivalents per year) between 1970 and 2010 representing about a quarter of all anthropogenic GHG emissions (Smith et al. 2014). Of these emissions, a significant portion originated from the sub-sector of Forestry and Other Land Use (FOLU) which includes Land Use Change (LUC, also referred to as land use and land-cover change using the abbreviation LULCC). It is estimated that deforestation and degradation of forests contributed about 12% of all anthropogenic GHG emissions between 1980 and 2010 (van der Werf et al. 2009).

It is widely accepted in the scientific community that avoiding the most catastrophic repercussions of climate change will require keeping the increase in global surface temperature below 2°C (IPCC 2014a). In the 'business as usual' scenario (i.e. continued positive flux of GHG emissions), the increase in temperature will likely exceed 4°C by the year 2100.

Therefore, any effective climate change mitigation policies and measures must include mechanisms to actively reduce emissions and increase sinks in the AFOLU sector, which must focus on reducing deforestation and forest degradation. Remote sensing presents an efficient and accurate means to detect deforestation and forest degradation over large areas. In many cases this allows for monitoring of forests at a scale that would be impractical with ground-based observations and measurements.

The UNFAO definition of forest requires a minimum 10% canopy cover and a minimum area of 0.5 Ha, with trees reaching a height of 5 meters or greater. Deforestation is defined as the conversion of forest to some other form of land use, which includes a permanent reduction in canopy cover to below 10%. Forest degradation is more difficult to define succinctly; it involves long term reduction of canopy cover due to human or natural activities but keeps the requirements for land cover classification of forest (i.e. the canopy cover remains above 10%). Forest degradation also implies a long-term reduction in the capacity of a forest to sustain biodiversity, provide resources, and sequester carbon from the atmosphere (UNFAO 2015).

The need to accurately measure activity data as related to forest clearing and degradation is essential for the implementation of REDD+ (Reduced Emissions from Deforestation and Degradation with the ‘plus’ symbolizing efforts to promote conservation, sustainable forestry, and enhancement of carbon stocks) (Corbera and Schroeder 2011). The IPCC defines activity data as a magnitude of the emissions or removals due to some human activity in a particular sector over a certain period of time. In the forestry sector, activity data may refer to measurements of area or area change of forested land. Overall emissions are calculated by multiplying an emission factor coefficient by the activity data. An emission factor coefficient therefore is some value which relates the activity data to a physical measurement of emissions (Houghton et al. 1997).

Miombo woodlands are the dominant forest type in Malawi. They are an ecosystem of particular concern due to recent increased rates of deforestation, which in turn drives GHG emissions as well as biodiversity loss. In the country of Malawi, Miombo woodlands are essential to the local population as a source of domestic energy (Abbot and Homewood 1999). The demand for fuelwood has driven encroachment of wood harvesting into Malawi's protected forests as other sources have become depleted. As local sources become depleted, those responsible for collecting fuel wood for their households must travel increasingly farther abroad into the wilderness to find good quality wood (Brouwer, Hoorweg, and van Liere 1997).

In addition to mitigating greenhouse gases, forests and woodlands in Malawi play an essential role in water quality and soil retention. Expanding agriculture contributes to increased run-off, which in turn increases the amount of suspended solids and nutrients entering water bodies. Studies have been done using remote sensing products to quantify the relationship between conversion of Miombo to negative impacts on water supplies. To provide improved information for land management practices in the Upper Shire River Catchment Palamuleni et al used Landsat data to map land cover change. Imagery from 1989 and 2002 was processed using a maximum likelihood classifier to identify land cover types spatially. The authors used these data to show that cultivated land increased while savanna, shrubs, and woodlands showed a decrease in cover area. These changes in land cover were found to directly contribute to negative water impacts in the Upper Shire river catchment, such as increased run-off and degradation of ground-water supplies during the dry season (Palamuleni et al. 2011).

In Malawi, deforestation occurred at a rate of 3.5% from the mid 1970's to the mid 1980's driven by expanding agriculture. Fuel wood use was also a major contributing factor during this time period. A study using AVHRR and MODIS NDVI to determine which land cover types were being converted to agriculture in the time period of the 1980's to 2005 (Chavula, Brezonik, and Bauer 2011). The study found that savanna and woodland experienced significant loss due to agricultural expansion from 1982-1995, but then a slight increase in this land cover type was observed from 1995 to 2005. They did concede the caveat of comparing AVHRR and MODIS due to the difference in resolutions (8km resolution for AVHRR compared to 500m resolution for MODIS). These large differences in resolution make it difficult to make meaningful comparison in vegetation cover at the smaller MODIS scale.

Other remote sensing work has been done to map land cover for the entire country of Malawi. One such study compared the efforts of 4 separate methodologies carried out by different teams to map land cover and land use change in Malawi to assist with greenhouse gas reporting (Haack, Mahabir, and Kerkering 2015). This review showed that each of the individual assessments produced different results in land cover change, due to differences in methods. This highlights the challenge of developing significant and reproducible remote sensing analysis of forest cover in Malawi.

Hudak and Wessman used NDVI derived from 4 Landsat MSS imagery and field measurements to estimate changes in woody canopy cover from the satellite data. A mean NDVI value from one of the dates was used to normalize NDVI for the other imagery to enable meaningful comparison between the different images.   Overall, they found a 1.8% reduction in woody canopy between 1981 and 1992 (Hudak and Wessman 2000).

There has been very little work on measuring degradation of open canopy woodlands and specifically Miombo woodlands in Malawi at the national scale. Most of the remote sensing work to date has focused on closed canopy forests; this work has been shown to be both accurate and effective for detecting change in these types of forests. Open canopy woodlands are more difficult to observe change in due to the presence of background soil signal in remote sensing data and other factors such as seasonality (e.g. differences in canopy during wet vs. dry seasons). Detecting change in open canopy woodlands is vital to REDD+ efforts which require activity data for these regions, especially in countries such as Malawi whose forest lands are dominated by this type of vegetation. Furthermore, detecting change within open canopy woodlands in which the land cover itself does not change is also important for developing activity data. This change is referred to as forest degradation and in countries such as Malawi represents a decrease in the woodland's ability to conduct primary production and sequester carbon, which is why it is vital to national REDD+ efforts. The aim of the research of this thesis has been to use Landsat data to demonstrate the feasibility of mapping of degradation and deforestation in sparse woodland systems at the national scale to support Malawi's nation REDD+ Program. Furthermore, this research seeks to demonstrate a technique for detecting forest degradation at the national level, which could be deployed by nations using freely available data and technologies. REDD+ efforts in Malawi will be better informed by an accurate method to provide reliable woodland degradation monitoring and mapping. These methods could then inform efforts to produce national estimates of emissions and removals from activity data, as one component of a National Forest Monitoring System. The goals of this thesis are therefore to provide the technical groundwork for conducting analysis of degradation of Miombo woodlands, demonstrate the usefulness of using freely available Landsat imagery as the source of analysis data, and to provide spatial locations and area estimates of degraded or deforested Miombo in Malawi. The techniques and data produced by this study will provide actionable scientific data and methodologies for the Malawi PERFORM project, which is a mechanism for assisting Malawi with preparing for REDD+. The areas of interest for this study are specifically those gazetted as protected forest lands in the country of Malawi.

Chapter 2: Methods

I: Using Landsat Medium Resolution Data

The Landsat data archive provides an invaluable source of earth observations which are ideal for studying land cover change for various reasons. Landsat satellites have acquired imagery for most of the earth's landmasses on a regular basis from 1972 up to the present day. Imagery is collected and made available to the public free of charge via the USGS Earth Resources Observation and Science Center (EROS) (Wulder et al. 2012; Woodcock et al. 2008). All Landsat data used in this study were acquired from the USGS EROS data archive using the Global Visualization Viewer (GLOVIS) Tool (http://glovis.usgs.gov).

	Landsat 5	Landsat 7	Landsat 8
Sensor	Thematic Mapper	Enhanced Thematic Mapper Plus	Operational Land Imager and Thermal Infrared Sensor
Beginning Date of Operation	March 1984	April 1999	April 2013
End Date of Operation	November 2011	Still in Operation[1]	Still in Operation
Repeat Time	16 days	16 days[2]	16 days[2]

Table 1: Descriptive information for the Landsat satellites used for this study.

[1] Landsat 7 ETM+ imagery collected since May 2013 has gaps of missing data due to the failure of an on-board mechanism responsible for correcting the forward motion of the spacecraft.

[2]The repeat times for Landsat 8 and Landsat 7 are 16 days, but they are in a staggered orbit allowing for a scene to be visited every 8 days

The Thematic Mapper (TM) sensor was deployed on Landsat 5 in March 1984, and was operational until November 2011. The Enhanced Thematic Mapper Plus (ETM+) sensor was deployed on Landsat 7 (Landsat 6 was launched in October 1993 but failed to reach orbit) in April 1999. On May 31, 2003 the scan-line corrector (SLC) on Landsat 7, which adjusted the instrument for the forward motion of the spacecraft, experienced a failure that causes all imagery collected since to have missing strips of data. Although the data collected after the SLC failure is still radiometrically useful, it is difficult to use in change studies due to the significant areas of imagery missing (Wulder et al. 2008; Williams, Goward, and Arvidson 2006). For this reason imagery categorized as "SLC-off" was avoided when possible. Most recently, the Operational Land Imager (OLI) deployed on-board the Landsat 8 platform was launched in February 2013 and is fully operational (Irons, Dwyer, and Barsi 2012).

The spatial resolutions for the TM sensor, ETM+ sensor, and OLI sensor are all 30 meters. This medium-scale resolution provides a consistent spatial measurement over time that is adequate for landscape-scale studies (Woodcock and Strahler 1987; Skole and Tucker 1993; Matthew C. Hansen and Loveland 2012).

Global coverage is provided by Landsat instruments on a 16-day period, so any given area of the earth is imaged once every 16 days by a single sensor, with the Landsat 7 ETM+ and Landsat 8 OLI sensors being the two that are currently active. Furthermore, Landsat 7 and Landsat 8 orbits are staggered by 8 days meaning that any area of the earth is imaged once every 8 days by these two platforms. Therefore, the temporal resolution of 16 days—and in some cases 8 days when the missing scan-line corrector data are acceptable—makes the Landsat data archive incredibly useful for earth monitoring.

The radiometric resolution of the sensors refers to the bit-depth which in turn gives an idea of how detailed the imagery is, or how many unique gray-levels are present in a single band of the image. TM and ETM+ sensors collect data at 8 bits meaning that each band can have a maximum of 256 gray levels, while OLI collects data at 12-bits giving it 4096 maximum gray levels per band. The 12-bit imagery is ideal due to its greater signal-to-noise ratio which is a result of the greater bit depth, but data from the OLI is only available since 2013, which is only part of the historical record of this study.

The spectral resolution of the TM, ETM+, and OLI sensors provide coverage in the visible, near-infrared (NIR), and short-wave infrared (SWIR) wavelengths. Each Landsat platform contains a thermal infrared imaging sensor, but these products are not used in this study. The visible, NIR, and SWIR portions of the electromagnetic spectrum are extremely useful for detecting different types of land cover (cf. vegetation, water, solid earth, snow and ice). This study focuses on vegetation cover, and the visible and NIR portions of the spectrum provide the most useful information and the coverage provided by all Landsat instruments is ideal for this purpose. Furthermore, radiometric calibrations have been well documented and this allows for the comparative analyses of imagery acquired from different Landsat platforms. The consistency of data acquisition and the ability to perform radiometric calibration allows for comparisons of imagery to accurately detect changes over space and time.

We use Landsat data for a specific application that involves measuring a parameter referred to as vegetation fractional cover—the percentage of canopy vegetation to bare substrate within a given pixel (Matricardi et al. 2007; Matricardi et al. 2010; Matricardi et al. 2013). The readily-available medium resolution satellite data from Landsat sensors represents a well-known and widely used tool for measuring forest cover change and also forest carbon stocks.

II: Data Acquisition for Malawi

The country of Malawi is covered by 11 nominal WRS-2 Landsat scenes from three paths and 6 rows of the Landsat World Reference System (Figure 1). Landsat imagery was acquired for each of the path/row combinations covering Malawi, resulting in full national coverage at three different general time periods – 2000 (±2), 2009 (±1) and 2015 (±1) (Tables 2, 3, & 4)). In order to perform a change analysis of Miombo woodlands, three epochs were selected for which to compare the fraction of vegetation cover over time. The use of epochal datasets comprising imagery that spans ± 2-3 years rather than single date acquisitions was necessary. There are a few reasons for this: cloud cover limits the availability of usable imagery at any given time, the coverage provided by Landsat sensors is periodic and clouds, haze, or smoke may severely limit the number of usable acquisitions, and in some instances scenes may not be available in the archive if they were not delivered to EROS from their original ground receiving stations. Three mosaic datasets were created covering the early dry season phenological period to study degradation and deforestation on the national scale for Malawi. This early phenological period of the dry season lasts from approximately May through the end of August. However, leaf senescence in some locations begins as early as July and reaches a maximum in August, so we target acquisitions between May and June. Imagery were selected with the aim of using the most temporally similar day-of-year (DOY) sets. All Landsat data were projected to the WGS 84 datum and UTM Zone 36 South projection, and clipped using a national boundary shapefile. This boundary shapefile was obtained from the Malawi Spatial Data Platform website (MASDAP 2013).

Images were organized in terms of individual paths, and the country of Malawi is covered by three WRS-2 paths: 167, 168 and 169. Paths correspond to the North-South direction of the satellite in orbit and therefore represent data that were collected in a single flyby. This means that scenes within an individual path can be collected on the same day of year with north and south adjacent scenes being acquired sequentially. This is advantageous because these data can be more seamlessly mosaicked and processed as a single path dataset due to the uniformity of atmospheric conditions and sun-earth-sensor geometry.

Path/Row	Image ID	Acquisition Date
169/67	LE71690672002128SGS00	5/8/2002
169/68	LE71690682002128SGS00	5/8/2002
169/69	LE71690692002128SGS00	5/8/2002
169/70	LE71690702002128SGS00	5/8/2002
169/70	LE71690702001125SGS00	5/5/2001
168/68	LT51680681998134JSA00	5/14/1998
168/68	LE71680682002153SGS00	6/2/2002
168/68	LT51680682001126JSA00	6/6/2001
168/69	LT51680691998134JSA00	5/14/1998
168/70	LT51680701998134JSA00	5/14/1998
168/71	LT51680711998134JSA00	5/14/1998
167/70	LE71670702002146SGS00	5/26/2002
167/71	LE71670712002146SGS00	5/26/2002
167/72	LE71670722002146SGS00	5/26/2002

Table 2: Landsat scenes used to create the 1998-2002 mosaic.

A note on naming conventions in the image IDs: ‘L’ refers to Landsat and the proceeding two characters represent the sensor. ‘E7’ represents the enhanced thematic mapper plus (ETM+) sensor onboard Landsat 7, ‘T5’ represents the thematic mapper (TM) onboard Landsat 5, and ‘C8’ represents the combined operational land imager (OLI) and thermal infrared sensor (TIRS) onboard Landsat 8. The next 6 digits represent the path and row in the format PPPRRR. The next 4 digits represent the year, and the next 3 digits represent the Julian day of year. The final characters in the image ID represent the receiving station and archive version number.

Path/Row	Image ID	Acquisition Date
169/67	LT51690672009155JSA02	6/4/2009
169/68	LT51690682009155JSA02	6/4/2009
169/69	LT51690692009155JSA02	6/4/2009
169/70	LT51690702009155JSA02	6/4/2009
168/68	LT51680682009164MLK00	6/13/2009
168/68	LT51680682008146JSA00	5/25/2008
168/68	LT51680682009148JSA02	5/28/2009
168/69	LT51680692009164MLK00	6/13/2009
168/69	LT51680692008178JSA00	6/26/2008
168/69	LT51680692009148JSA02	5/28/2009
168/69	LT51680692009180JSA02	6/29/2009
168/70	LT51680702009164MLK00	6/13/2009
168/70	LT51680702009148JSA02	5/28/2009
168/70	LT51680702009180JSA02	6/29/2009
168/71	LT51680712009148JSA02	5/28/2009
168/71	LT51680712008130JSA00	5/9/2008
167/70	LT51670702008155JSA01	6/3/2008
167/70	LT51670702009173JSA03	6/22/2009
167/71	LT51670712009157JSA02	6/6/2009
167/72	LT51670722008139MLK00	5/18/2008
167/72	LT51670722010128JSA00	5/8/2010
167/72	LT51670722008123JSA00	5/2/2008
167/72	LE71670722009149ASN00	5/29/2009

Table 3: Landsat scenes used to create the 2008-2010 mosaic.

Path/Row	Image ID (gap-fill order)	Acquisition Date
169/67	LC81690672015156LGN00	6/5/2015
169/67	LC81690672014137LGN00	5/17/2014
169/68	LC81690682015156LGN00	6/5/2015
169/68	LC81690682014137LGN00	5/17/2014
169/69	LC81690692015156LGN00	6/5/2015
169/70	LC81690702015156LGN00	6/5/2015
168/68	LC81680682014178LGN00	6/27/2014
168/68	LC81680682014130LGN00	5/10/2014
168/69	LC81680692015165LGN00	6/14/2015
168/69	LC81680692015133LGN00	5/13/2015
168/70	LC81680702015165LGN00	6/14/2015
168/70	LC81680702015133LGN00	5/13/2015
168/71	LC81680712015165LGN00	6/14/2015
168/71	LC81680712015133LGN00	5/13/2015
168/72	LC81680722015165LGN00	6/14/2015
167/70	LC81670702014155LGN00	6/14/2014
167/70	LC81670702015158LGN00	6/7/2015
167/71	LC81670712014155LGN00	6/14/2014
167/71	LC81670712015158LGN00	6/7/2015
167/72	LC81670722014155LGN00	6/14/2014
167/72	LC81670722015158LGN00	6/7/2015

Table 4: Landsat scenes used to create the 2014-2015 mosaic.

Paths adjacent to the east and west correspond to different flyby dates. Therefore the imagery of adjacent paths across a given East-West row will be slightly different in terms of reflectance due to differences in atmospheric conditions, climate conditions such as temperature and precipitation, and sun-earth-sensor geometry. Normalization of these differences was necessary to reduce patch-work results in the mosaic datasets. Normalization of an image is accomplished by using a simple linear regression model to relate one image to another image.

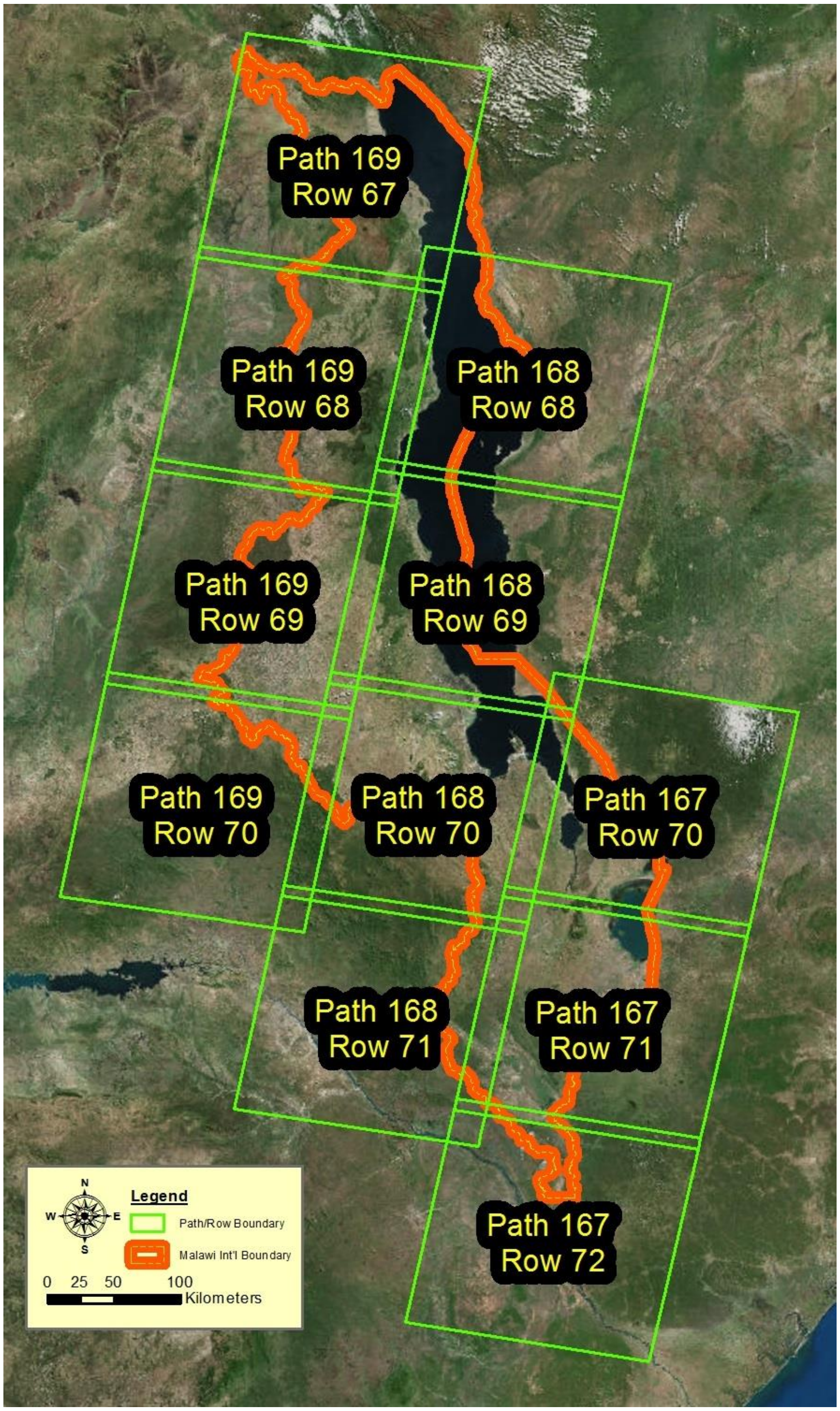

Figure 1: Malawi Path/Row Scenes. Malawi is covered by 11 nominal WRS-2 path/row scenes which are shown here overlaid onto the Malawi international border for reference.

Ideally these two images will overlap and cover some similar ground features that remain static between the two acquisitions. Reference points selected over these static areas can be used to generate the linear regression model that is used to estimate the normalization between the two input images (Elvidge et al. 1995; Matricardi et al. 2013). Epoch 1 for the early dry season mosaic consists of imagery acquired in May of 1998 and 2002, epoch 2 was comprised of imagery collected in May and June of 2008 and 2010, and epoch 3 is comprised of imagery acquired in May 2014 and 2015.

III: Workflow

Raw Landsat data were acquired using the USGS GLOVIS online tool (http://glovis.usgs.gov). Individual path/row scene multispectral datasets were first converted to at-sensor-radiance from the raw digital numbers (DNs), and then converted to top of atmosphere (TOA) reflectance by using the scene specific gain/offsets, scene specific solar elevation angles and sun-earth distance along with sensor-specific exoatmospheric spectral irradiances using the following equations (Chander, Markham, and Helder 2009):

Convert raw DNs to spectral radiance:

$$L_{\lambda} = \left(\frac{\mathrm{LMAX}_{\lambda} - \mathrm{LMIN}_{\lambda}}{\mathrm{Q}_{\mathrm{calmax}} - \mathrm{Q}_{\mathrm{calmin}}}\right) * (\mathrm{Q}_{\mathrm{cal}} - \mathrm{Q}_{\mathrm{calmin}}) + \mathrm{LMIN}_{\lambda}$$

Convert spectral radiance to TOA reflectance:

$$\rho_{\lambda} = \frac{\pi * L_{\lambda} * d^2}{\mathrm{ESUN}_{\lambda} * \cos\theta_s}$$

Clouds, cloud shadows, and water were detected and masked for each scene by using the fmask algorithm. Fmask, which stands for function of mask, is a completely self-contained algorithm that uses an input Landsat scene to generate a thematic product which identifies each pixel as clear land, water, cloud, cloud shadow, or snow. This is advantageous since no other ancillary data or scene-specific parameterization is required to generate the mask, allowing for a more streamlined and efficient method of cloud and cloud-shadow detection. Fmask works by taking advantage of known physical and spectral properties of clouds to identify potential cloud pixels. Cloud shadows are identified using spectral characteristics with the near infrared band and the satellite viewing angle to accurately estimate shadow placement (Zhu and Woodcock 2012). Each mask was applied to its parent Landsat scene to recode as 0 any pixels that were flagged as cloud, cloud shadow, or water. Furthermore, a buffer of 10 pixels surrounding any flagged pixel was used to remove any potentially undetected "boundary" pixels. A serious caveat of using 10 pixels as a buffer is that there is a very likely increase in commission error causing usable clear-land pixels to be ignored. This was mostly relevant for detected cloud and cloud shadow pixels, since clouds can have hazy pixels immediately surrounding them that are not detected by the algorithm, which themselves can cast a shadow that lowers the reflectance in the vicinity of the corresponding cloud-shadow. The 10-pixel buffer helps to minimize the inclusion of contaminated pixels in the final masked products.

The TOA reflectance conversion corrects for differences in sensor offsets and gains, solar zenith angles, sun-earth distance, and solar irradiances at the different times of acquisition. However, the TOA reflectance data still suffer from atmospheric interference that causes scattering, absorption, and refraction of light between the earth surface and the satellite sensor. There are numerous atmospheric correction methods which exist in varying degrees of complexity. A radiative transfer model such as the 6S (Second Simulation of the Satellite Signal in the Solar Spectrum) attempts to account for this atmospheric interference to obtain a true surface reflectance (Vermote et al. 1997). Models such as these are incredibly complex and oftentimes require image-specific ancillary data such as the aerosol optical thickness (AOT) to produce accurate results. AOT is measured by ground-based weather stations and is not available at the necessary spatial or temporal distribution required to cover a single Landsat image due to the highly variable nature of the atmosphere—both over space and time. A highly detailed and complex AOT correction was therefore not used for this study.

On the other hand, other methods exist that approximate an atmospheric correction. Such methods are not as accurate but are much simpler to apply to such a large dataset as was used in this study. A dark object subtraction (DOS) technique was therefore employed to account for the additive nature of atmospheric interference (Chavez Jr. 1988). Using the information within each individual image, it is possible to identify this effect and minimize it by calculating band-specific correction factors. A starting band value in the visible spectrum was selected first, and then the accompanying band correction factors were calculated from this starting value based on a relative scattering model (Chavez 1996). The DOS technique can be easily applied to the imagery and was therefore chosen to produce the surface reflectance data for this study.

Surface reflectance datasets for each epoch were then mosaicked by path, and gap-filling of masked pixels was accomplished where multiple seasonally homogenous images were available. All of the images used for this process are listed in Tables 2, 3, and 4. The 3 path datasets for each epoch were combined into a national mosaic using an averaging function for overlap areas to minimize contrast between adjacent paths. The averaging function was a method of normalization by which a simple linear regression is applied to the overlap region of two adjacent scenes. These mosaic datasets were then clipped to the Malawi national boundary to produce the final multispectral national mosaic for each epoch.

A Normalized Difference Vegetation Index (see Chapter 3 Section II for description of this calculation) was calculated from the multispectral path mosaics rather than from the national mosaics due to differences between adjacent paths that become apparent when combining them into a single dataset. As mentioned above, adjacent paths do not mosaic seamlessly due to slightly different levels of greenness resulting from differences in acquisition dates. This can have deleterious effects for the national mosaic change algorithm results by causing an unnatural patch-working effect. To reduce this variability a scaling process was applied to the vegetation index path datasets to minimize false change detection owing to variations in pixel values for adjacent paths. The scaling process mentioned here is the normalization by means of regression modeling using sample points of static surface targets that are present in the two input scenes or mosaics.

A built-in random point generator for ArcMap (*ArcGIS for Desktop* (version 10.2.2) 2015) was used to generate 1000 random sample points with a minimum spacing of 120 meters. The location of all points was constrained using a polygon boundary that covered the spatial extent of each path-overlap area. This polygon was manually digitized using ArcMap. The vegetation index pixel values were extracted at each point location from the path datasets and added to the attribute table of the random points vector file. A column of pixel values was created for each path, and the values in each row represent the pixel values for an identical location shared by each path dataset allowing for the values at each location to be analyzed. The columns were copied from the ArcMap attribute table into an Excel spreadsheet to perform regression analysis. Path-to-path scaling was accomplished by identifying areas within the overlap of adjacent paths for which no the NDVI change was less than 20 percent. This was done to filter out areas where the change in NDVI was more likely to be the result of an actual land-cover change, rather than the result from atmospheric effects. It can be assumed that the vegetation index values for these areas should be nearly identical and that any difference is the result of differing conditions at the time of acquisition rather than differences in vegetation cover (Hudak and Wessman 2000). Mosaicking the scaled path dataset with the reference path dataset allowed for a visual inspection of the success of the scaling effort. The 3 paths were then mosaicked together and clipped to the Malawi national boundary to create the national NDVI datasets for each time period.

The NDVI was used in the calculation of vegetation fractional cover (*f*C). The fractional cover un-mixes the NDVI pixels between two pure components: vegetation and bare soil. Therefore, the final result is a continuous fields raster dataset in which each pixel represents the proportion of pure vegetation on a scale from 0-1. This is then rescaled to 0-100 to represent percentage vegetation cover by multiplying the *f*C by 100.

NDVI provide a relative abundance of vegetation within each pixel as compared to other signal contributors (e.g. soil) within the pixel. Vegetation indices such as NDVI therefore don't provide a physical measurement of vegetation, but rather are representations of the ratios between particular bands of remote sensing data (Carlson and Ripley 1997). Spectral mixture analysis (SMA) has been shown to provide a more accurate representation of vegetation on the ground than simply using NDVI (Elmore, et al. 2000). A continuous fields product that quantifies a gradient of vegetation abundance across space and is comparable over time is the proposed product for the detection of miombo degradation in this thesis. To achieve this, a spectral un-mixing method similar to SMA was employed to determine the percent abundance of vegetation in each pixel. This improves upon the information provided by NDVI by separating out the signal components within a pixel and provides continuous fields data that estimate the physical abundance of vegetation as a percentage within each pixel. The usefulness of these data for detecting degradation is that percentage quantities can be compared over time to determine if the relative abundance of vegetation at a given pixel has decreased. This is an improvement over simply classifying the spectral data into thematic cover types and comparing classes for a given pixel over time (i.e. a methodology useful for the detection of closed canopy deforestation). As described earlier, degradation occurs when there is a negative impact on a forest's capacity for primary production while still maintaining the same land cover type. This type of change would not be apparent when comparing thematic class types across time; rather it would be measurable when comparing the percentage abundance of vegetation over time. Therefore, NDVI was used as an input to a two-endmember SMA to generate continuous fields products that provide the abundance of vegetation as a percentage within each pixel. The two-endmember approach uses NDVI to separate the signal components of the NDVI value into a vegetation and non-vegetation percentage. This process is described in greater detail in Chapter 3 Section III.

Visual analysis was used to generate endmember sample areas for each path that represented pure Miombo and pure bare substrate pixels that remained consistent across all time periods and seasons. Areas of interest (AOIs) were drawn in ERDAS Imagine (*ERDAS Imagine* 2014) for these endmember sample areas. The pixel values were then collected from the AOIs using the Spectral Signature tool in ERDAS Imagine. The values sampled for each endmember were combined to calculate the average national dataset endmember values. These values were then entered into the fractional cover model to calculate *f*C at the national scale for each time period.

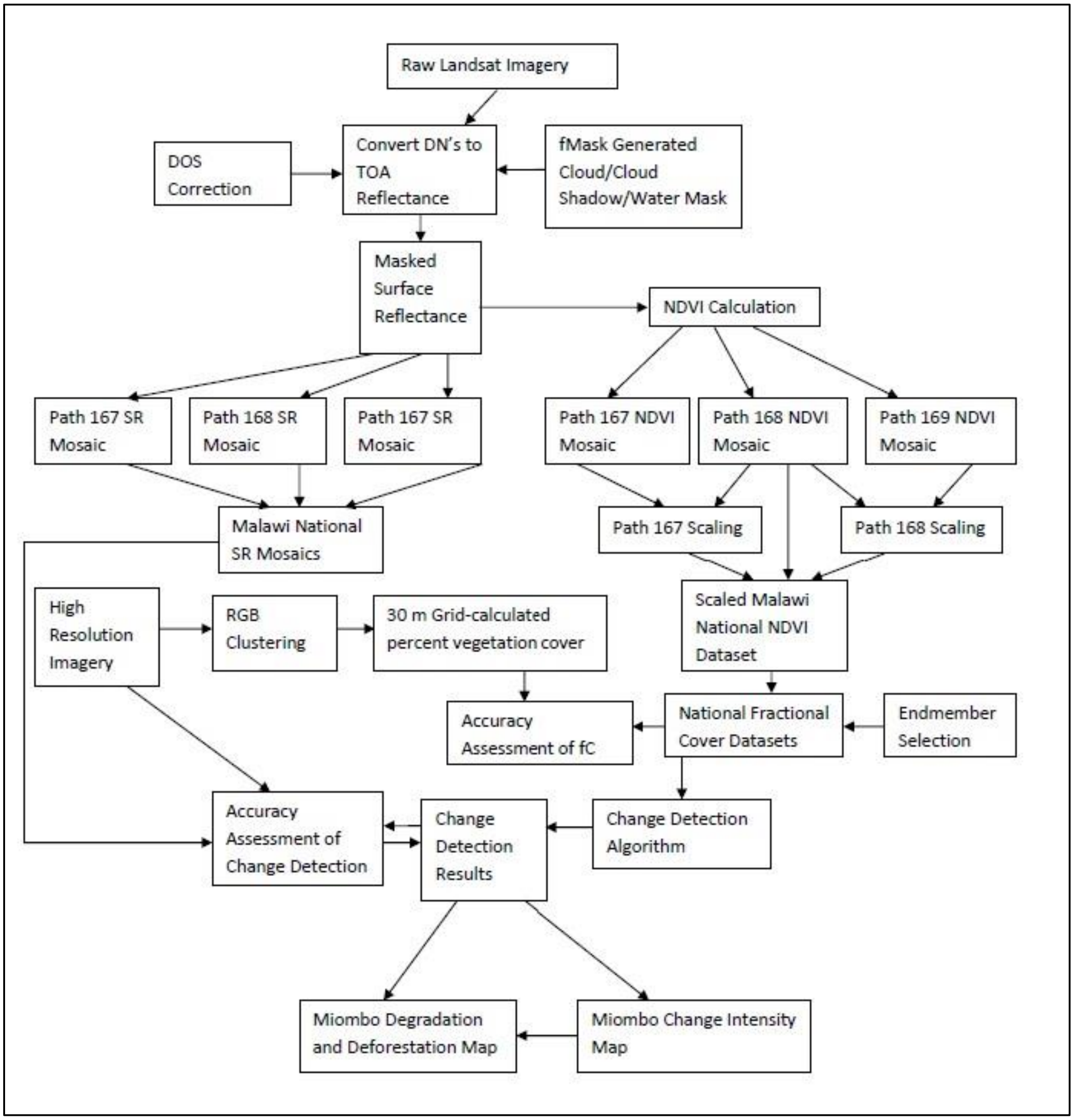

Figure 2: Flowchart showing the workflow used to generate the national-scale datasets and change results

Chapter 3: Results

I. National Multispectral Mosaics

A national multispectral mosaic was generated for each of the three time periods. The purpose of these is more for reference purposes, but they were also used for some of the change detection assessment. The mosaics were stitched together using an averaging function, wherein the mean value of overlapping pixels in adjacent paths of images was used in order to reduce the patchwork effect between adjacent paths. Histogram matching was also employed to further normalize the multispectral imagery by using path 169 as the reference dataset. Also, the surface reflectance datasets calculated with the DOS technique were used as the source of the mosaic components.

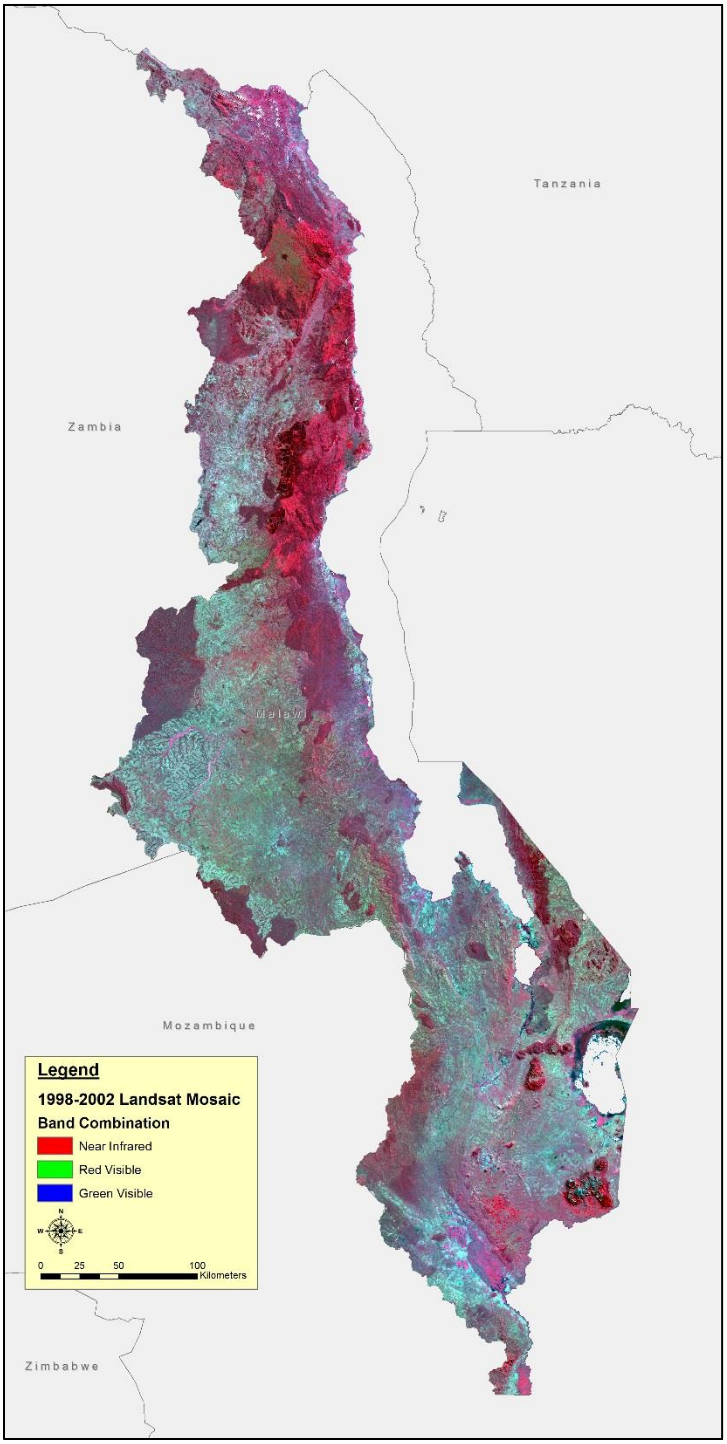

Figure 3: The 1998-2002 multispectral mosaic. The image is comprised of TM and ETM+ images stitched together using an averaging function for overlap areas and path to path histogram matching to reduce seamlines.

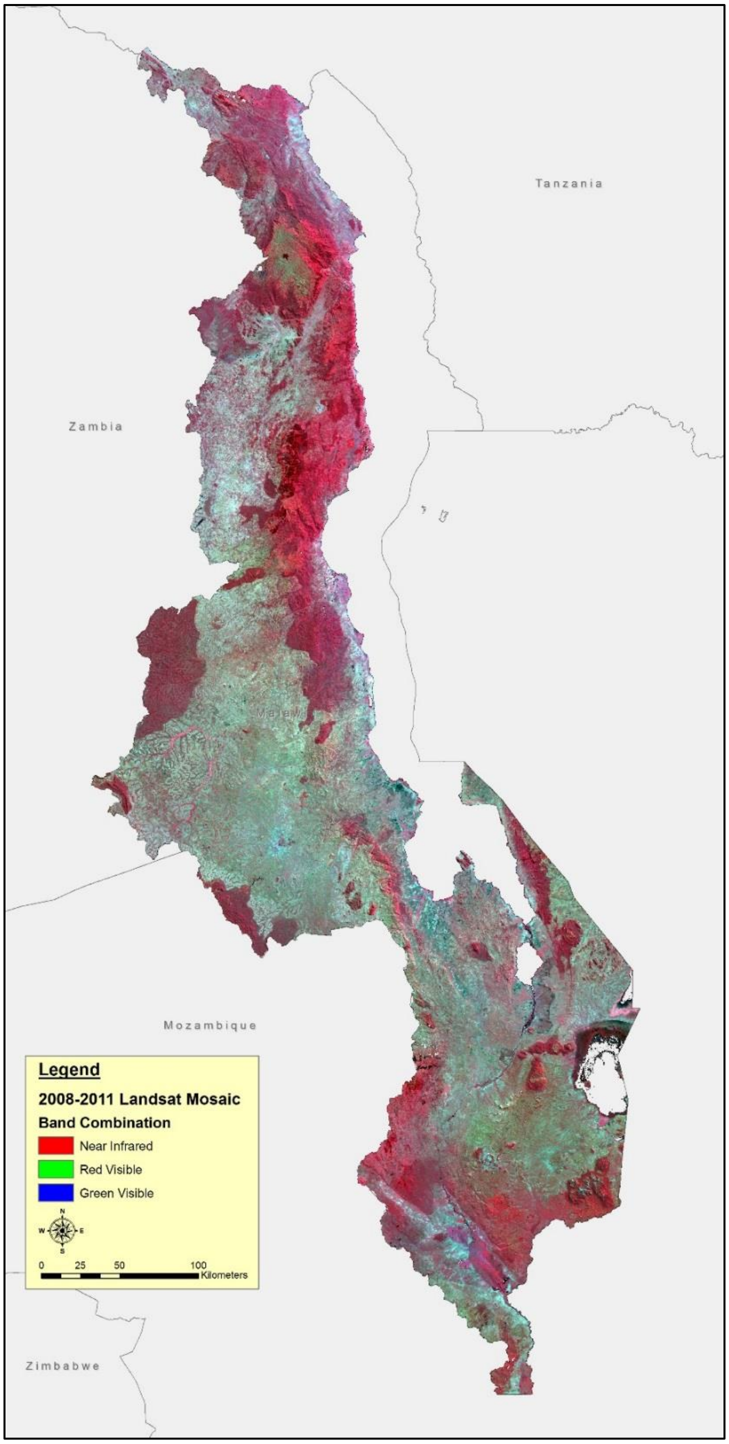

Figure 4: The 2008-2011 multispectral mosaic is composed almost entirely of TM imagery due to the SLC-off error on the ETM+ sensor for this time period. One ETM+ SLC-off image was used for gap-filling path/row 167/72. An averaging function was applied to overlap areas and no histogram matching was required.

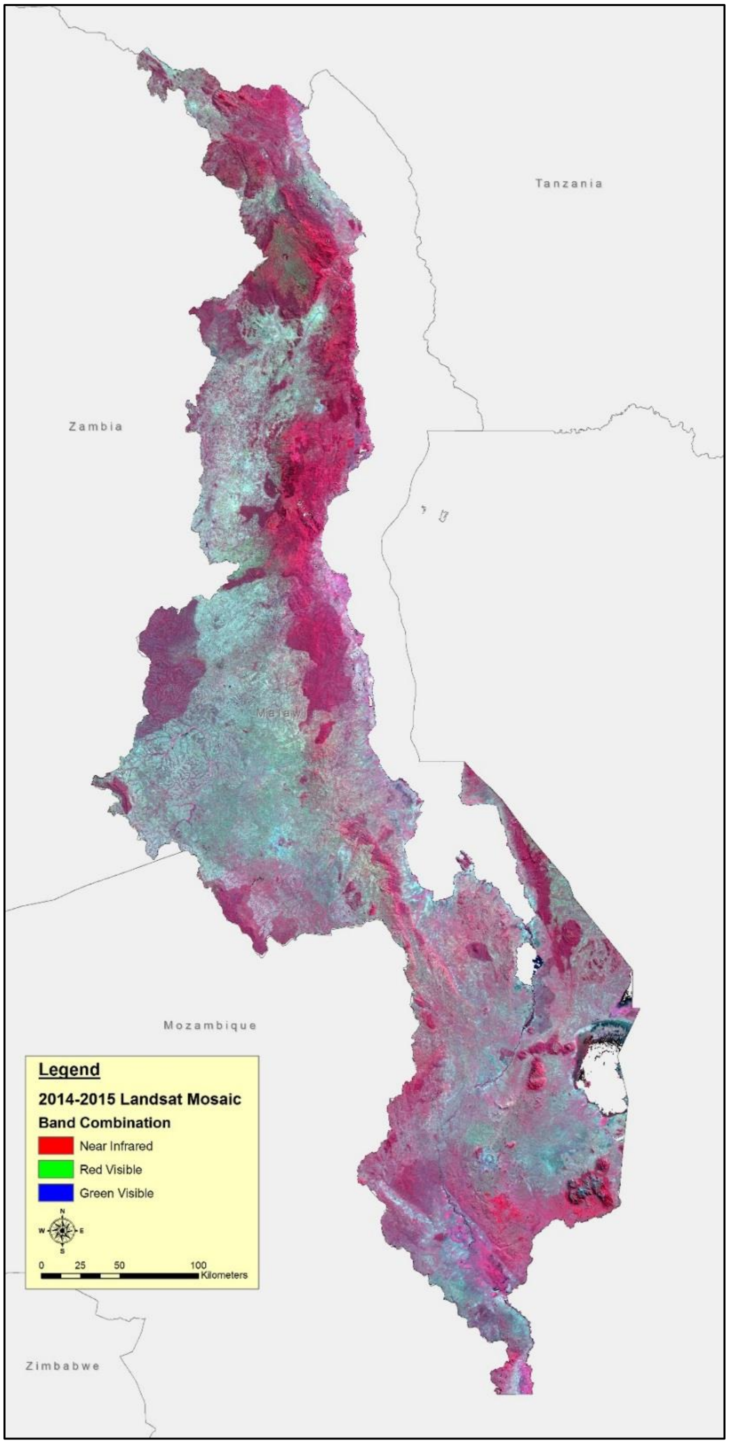

Figure 5: The 2014-2015 multispectral mosaic is composed entirely of OLI imagery. An averaging function was used for overlap areas and no histogram matching was required.

II. National NDVI Mosaics

Plant physiology has unique properties which allows remote sensing of plant characteristics. Photosynthesis causes plant leaves to be highly absorptive of the visible red portion of the electromagnetic spectrum. Also, the physical structure of plant leaves makes them highly reflective of the near infrared portion of the electromagnetic spectrum. A healthy tree canopy will therefore absorb most of the red visible light it receives for use in primary production while simultaneously reflecting much of the near-infrared light that also strikes it (Tucker 1979). These spectral characteristics are nearly unique to plants and photosynthesis and can be used to easily detect the presence of vegetation, measure the extent of plant coverage, or even estimate primary production via remote sensing. The red and near-infrared (NIR) reflectances of a surface can be plotted on an orthogonal axis to create what is referred to as a feature space image. This plot visualizes the similarity and variation between two bands. Since the red visible and near-infrared bands are sensitive to vegetation, portions of the plot between these bands correlate to either the presence of vegetation or bare soil. This helps explain the basis for vegetation indices and how they utilize the unique spectral characteristics of vegetation in the red-visible and near-infrared portions of the electromagnetic spectrum (Lillesand, Kiefer, and Chipman 2008).

A widely used vegetation index is the normalized difference vegetation index (NDVI). NDVI has historically been used as the index of choice for the study of vegetation dynamics in the field of remote sensing for decades. It is easily calculated from the red and near-infrared bands of satellite imagery, such as that acquired by Landsat, using the following equation:

$$NDVI = \frac{NIR - RED}{NIR + RED}$$

NIR and RED here refer to the reflectance values of the near-infrared and red bands respectively. NDVI has been shown to be directly correlated to biophysical characteristics of vegetation via a linear relationship with leaf area index (LAI) up to a particular value—generally between an LAI of 3 and 4 (Carlson and Ripley 1997). NDVI becomes insensitive to increases in LAI beyond a certain value, and therefore cannot measure differences in very dense canopies once LAI saturation has been reached (Tucker 1979). Therefore, NDVI may not be the best vegetation index for regions consisting of dense tropical canopies. Miombo, however, has characteristically open canopy making NDVI suitable for detecting the presence and vitality of Miombo woodlands (Frost 1996).

The NDVI mosaic datasets were calculated directly from the multispectral mosaic datasets using a graphical model in ERDAS Imagine. The goal of these was to represent a high quality record in time of the abundance of vegetation at the national scale. The values of NDVI range from -1 to 1, with 1 representing a higher abundance of "greenness". These datasets are displayed below in grayscale with darker regions corresponding to lower NDVI values and therefore lower abundances of vegetation. These datasets were used as direct inputs into the model used to calculate fC at the national scale using a simple two-endmember linear un-mixing algorithm.

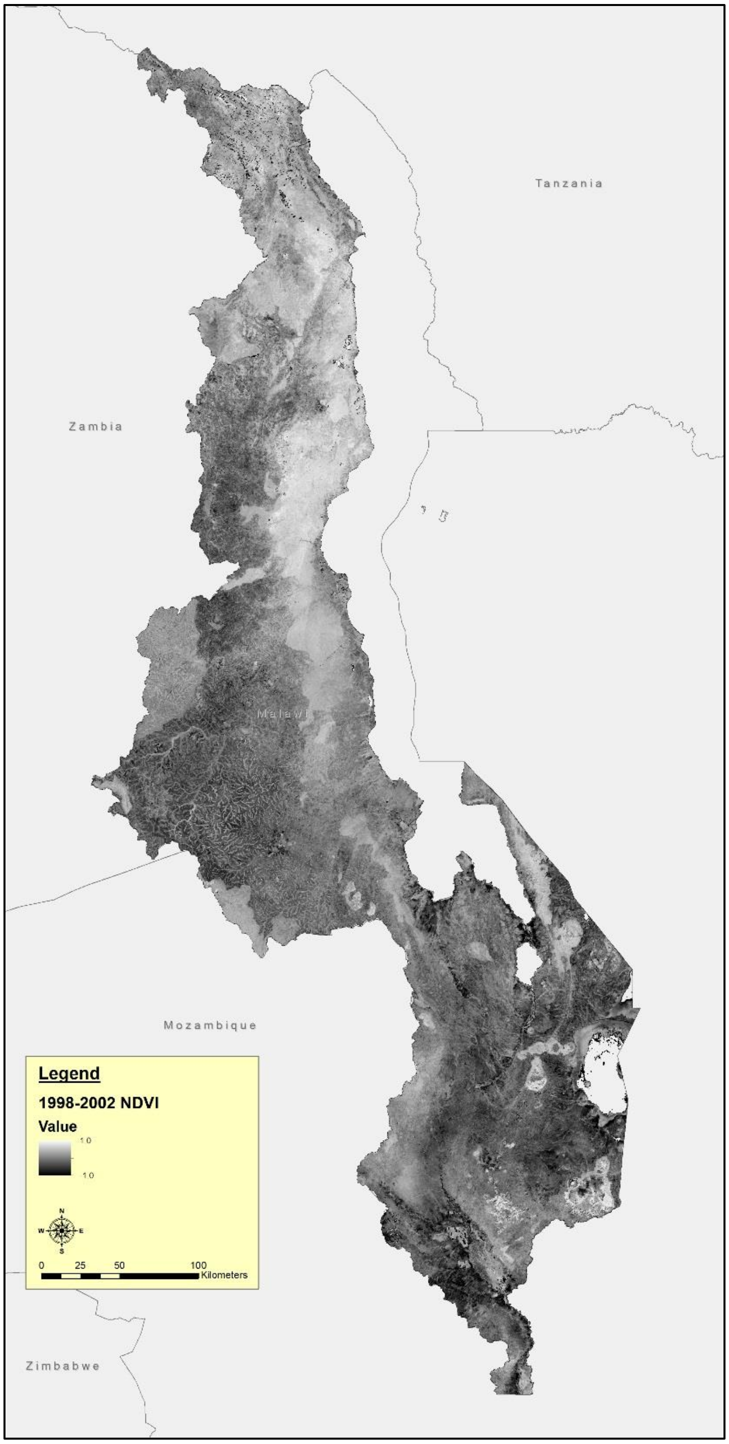

Figure 6: The national NDVI mosaic for the 1998-2002 time period.

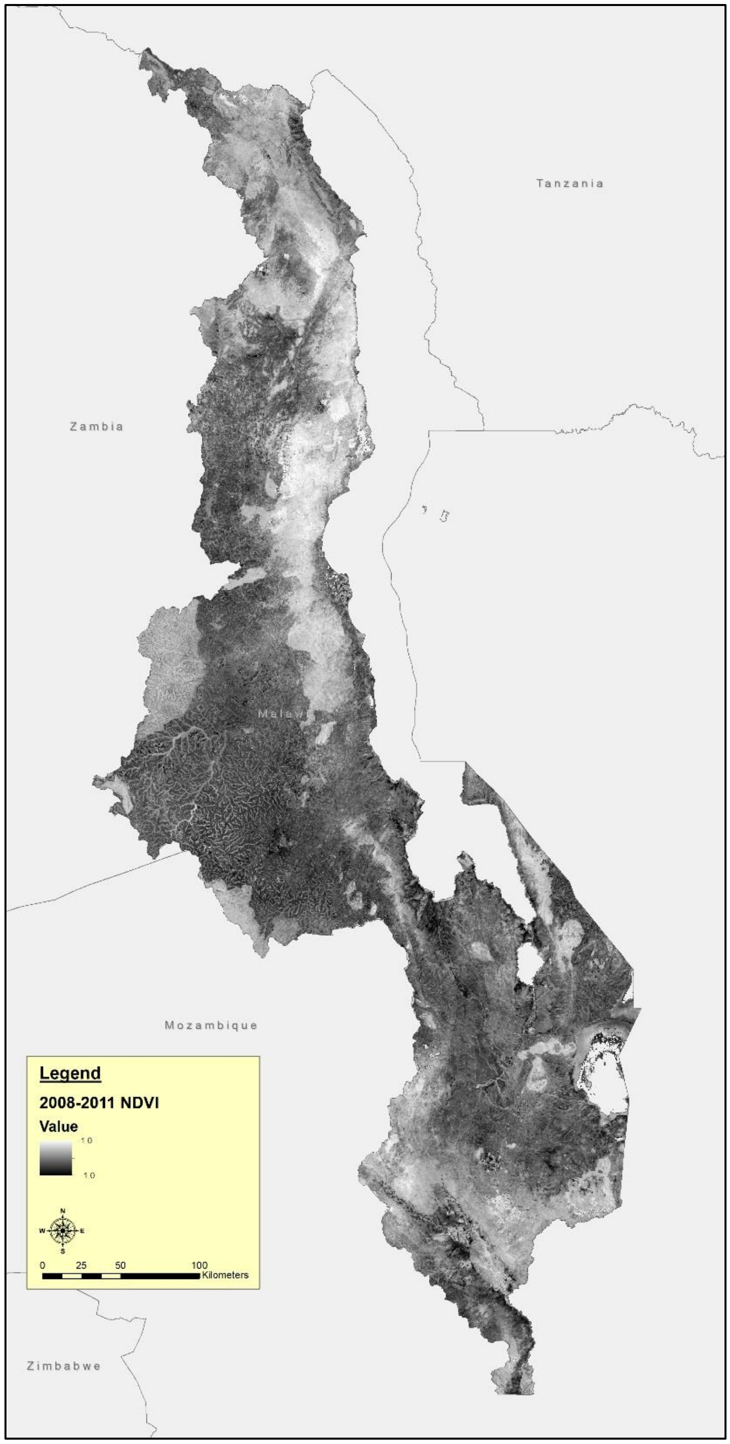

Figure 7: The national NDVI mosaic for the 2008-2010 time period.

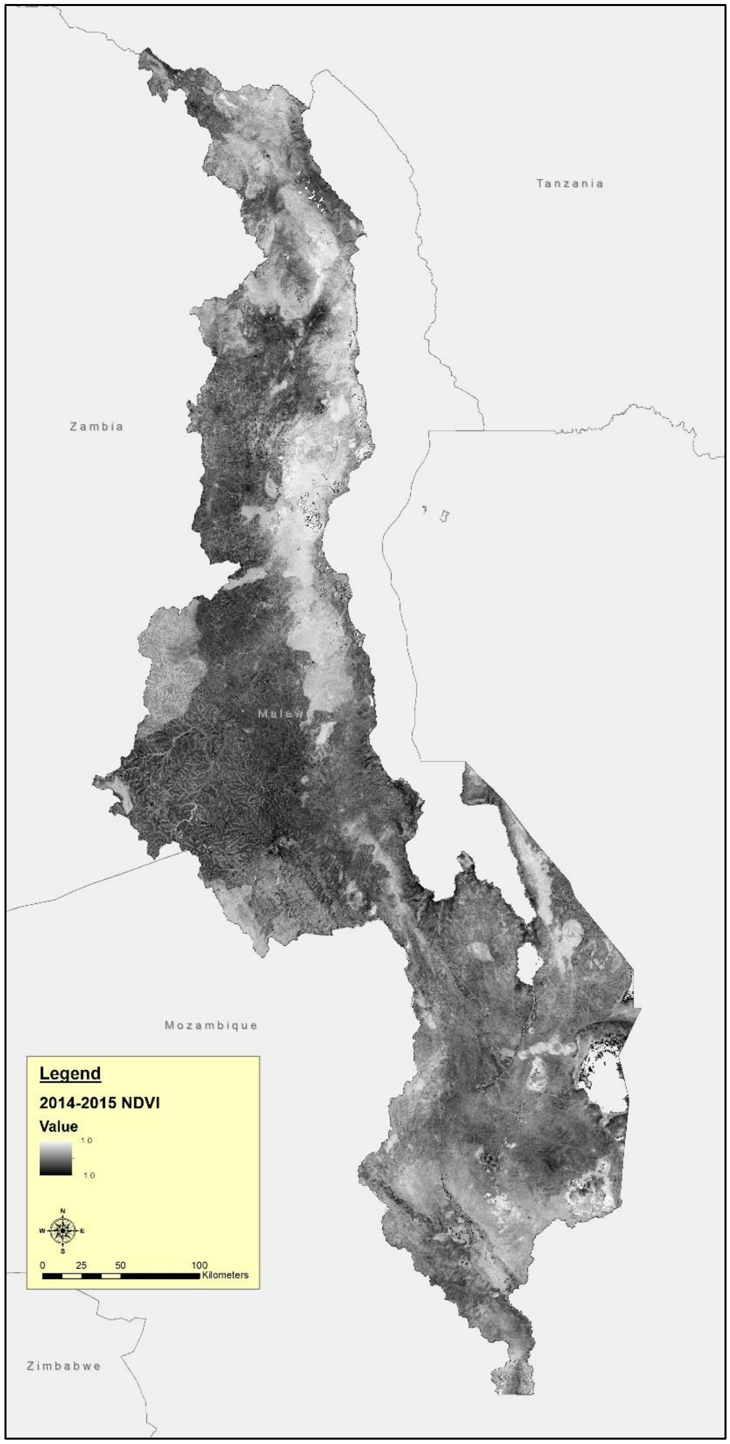

Figure 8: The national NDVI mosaic for the 2014-2015 time period.

III. National *fC* Datasets

The spatial resolution of Landsat is 30 meters, which provides a default minimum mapping unit that is ideal for regional studies. However, the area within a Landsat pixel, which is about 900 m^2, is relatively large for representing the measurement of a heterogenous land cover. Each pixel is potentially a mixture of land covers (e.g. canopy or soil) or land cover components (e.g. soil, green vegetation, shadow, stems and branches), all contributing to the overall reflectance signal. Thus, the reflectance signal for a given pixel is the sum of its land-covers or cover components. These sub-pixel land-cover elements can therefore be quantified at the pixel-scale using a measure of fractional cover, i.e. the percent for which each land cover type contributes to the pixel's reflectance signal for a particular wavelength, or range of wavelengths when speaking in terms of individual Landsat bands. Quantification of these land cover types across a landscape consistently is integral to the use of satellite imagery to measure change across time (Adams et al. 1995). There are a number of methods available for calculating fractional cover.

Spectral mixture analysis (SMA) is the process by which the fraction components within a pixel are calculated for a given band with given endmember values that are unique to each land cover type for each band. An endmember is simply the reflectance value for a particular homogenous land cover type at a particular wavelength or Landsat band. Therefore, SMA requires knowledge of not only the land cover types present within a pixel, but also each land cover type's endmember value at the given band. Also referred to as a linear spectral mixture analysis (LSMA), a typical scenario is separating vegetation such as forest from non-photosynthetic vegetation (NPV) and non-vegetation or bare soil (Cochrane and Souza 1998). An equation can then be used to describe the fraction component of each land cover type within the pixel and solved by combining a least-square estimator with the constraining factor that all fractions must sum to 1 for each pixel (Lillesand, Kiefer, and Chipman 2008).

Multiple endmember spectral mixture analysis (MESMA) builds upon SMA by charging that endmember values are variable throughout a satellite image (Roberts et al. 1998). MESMA therefore accounts for this extra variation in an attempt to generate a more accurate fractional cover, but requires more field data measurements to model the variation of endmember types across the landscape. MESMA is therefore a much more labor and computationally intensive algorithm best suited for very specialized scenarios for which extensive knowledge of the component reflectance characteristics exists.

These two methods – SMA and MESMA -- were employed to calculate the fraction of land cover types for multispectral data. This requires a great deal of computing and also requires determining several endmember values for each of the different land cover types. The number of bands in the image typically determines the maximum number of endmembers required (Lillesand, Kiefer, and Chipman 2008). The SMA approach used with multispectral imagery can be simplified by applying a linear un-mixing model to a vegetation index (Qi et al. 2000; Xiao and Moody 2005; Matricardi et al. 2010). As described previously, vegetation indices take advantage of the unique spectral characteristics of vegetation—generally in the visible red and near infrared portions of the electromagnetic spectrum—to describe the level of “greenness” present in an image. A linear un-mixing model uses a pure vegetation endmember and a pure bare soil endmember to calculate the fraction of vegetation present in each pixel with the following formula:

$$fC = \frac{VI - VI_{bare}}{VI_{veg} - VI_{bare}} * 100$$

Where VI is the value of the input vegetation index, VI_{bare} is the endmember vegetation index for bare substrate, and VI_{veg} is the endmember vegetation index for vegetation. The result is a raster file of continuous-.

Selecting the best representative endmembers for pure land-cover types is essential for correctly un-mixing the materials of interest within each pixel. There may be many different vegetation types within a Landsat scene. However, the location of Miombo in the study area is well documented. This allowed for accurately selecting pure pixels for determining endmembers associated with Miombo vegetation. To ensure consistency between fractional cover datasets, endmember samples were taken from identical areas of interest (AOIs) for both time periods. This was done to minimize the effects of atmospheric scattering due to haze and effects due to phenology as a result of meteorological or atmospheric differences across the two dates. This was because while both time periods are consistent in terms of seasonality and day of year (DOY) they may still exhibit slight differences due to these aforementioned factors. Similarly, for bare substrate endmembers, samples were taken from the same AOIs across both time periods for areas that were consistently bare, such as roads and large barren agriculture fields. Endmembers were sampled from each of the paths of Landsat imagery in or around the three principle study areas identified by the Malawi PERFORM project. These are the Perekezi, Ntchisi, and Liwonde forest reserves.

The three national *fC* datasets were produced directly from the national NDVI mosaic datasets. Endmembers were selected from each NDVI mosaic which represented pure vegetation and pure bare soil land cover types. These were found by selecting areas of the image that represented these pure land covers by drawing polygons around the areas of interest. The signature editor tool in ERDAS was then used to collect the NDVI values within each polygon.

The signature editor tool allowed for the calculation of the overall mean for each endmember value by combining the area of interest samples associated with each land cover type. The tool also allowed for the verification of quality samples by the use of histograms to ensure samples had a normal distribution. Once the endmembers were determined, they were input into an ERDAS graphical model which calculated the *f*C directly from the NDVI mosaic dataset. This produced a national *f*C dataset for each time period.

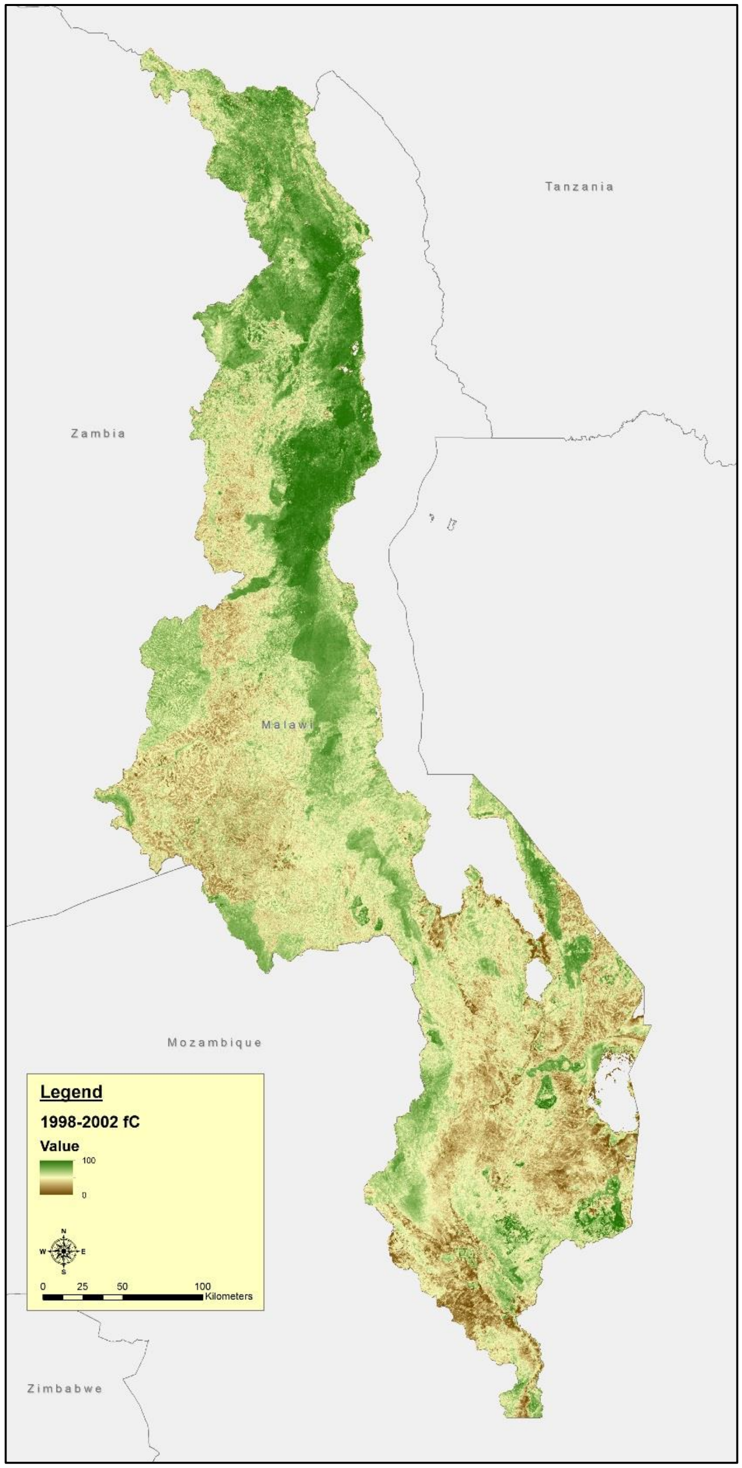

Figure 9: The national *f*C dataset for the time period of 1998-2002.

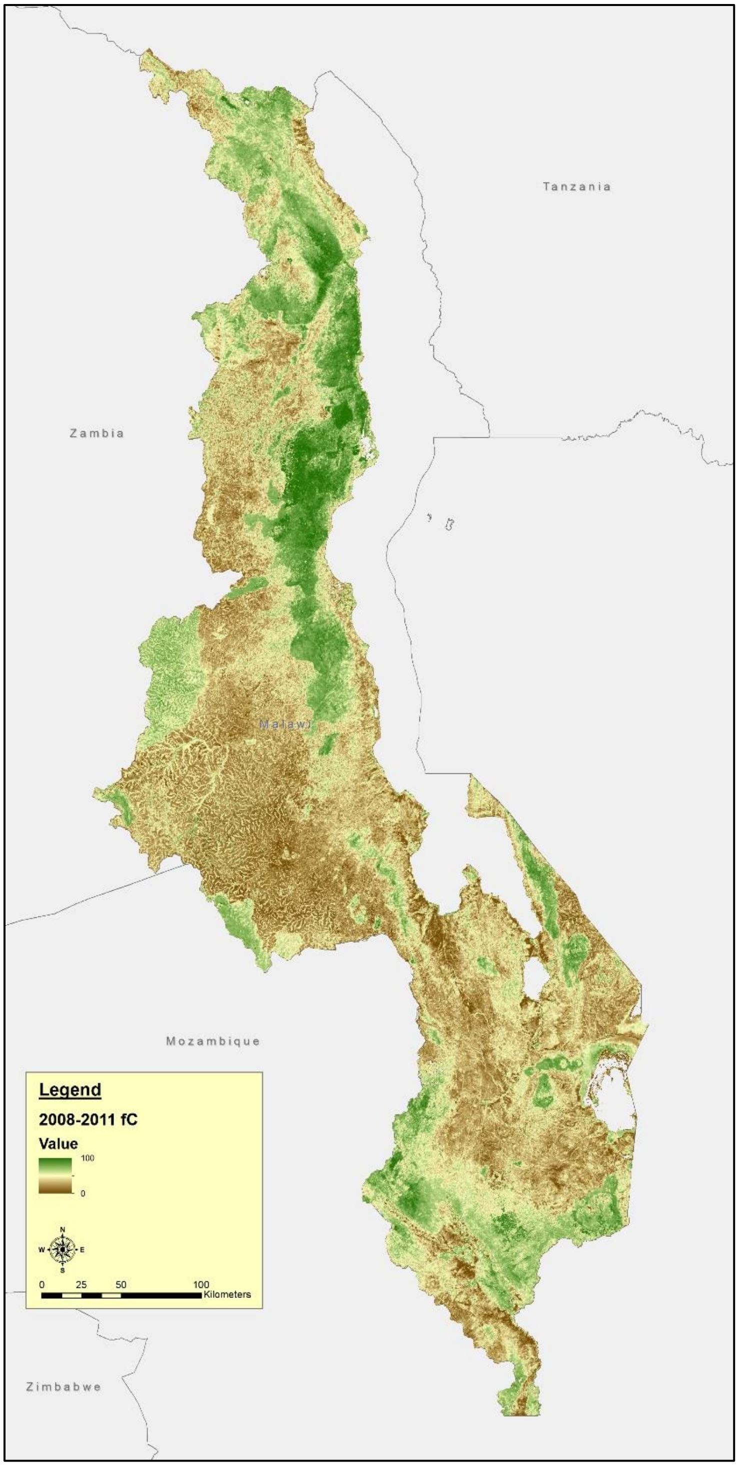

Figure 10: The national *f*C dataset for the time period of 2008-2010.

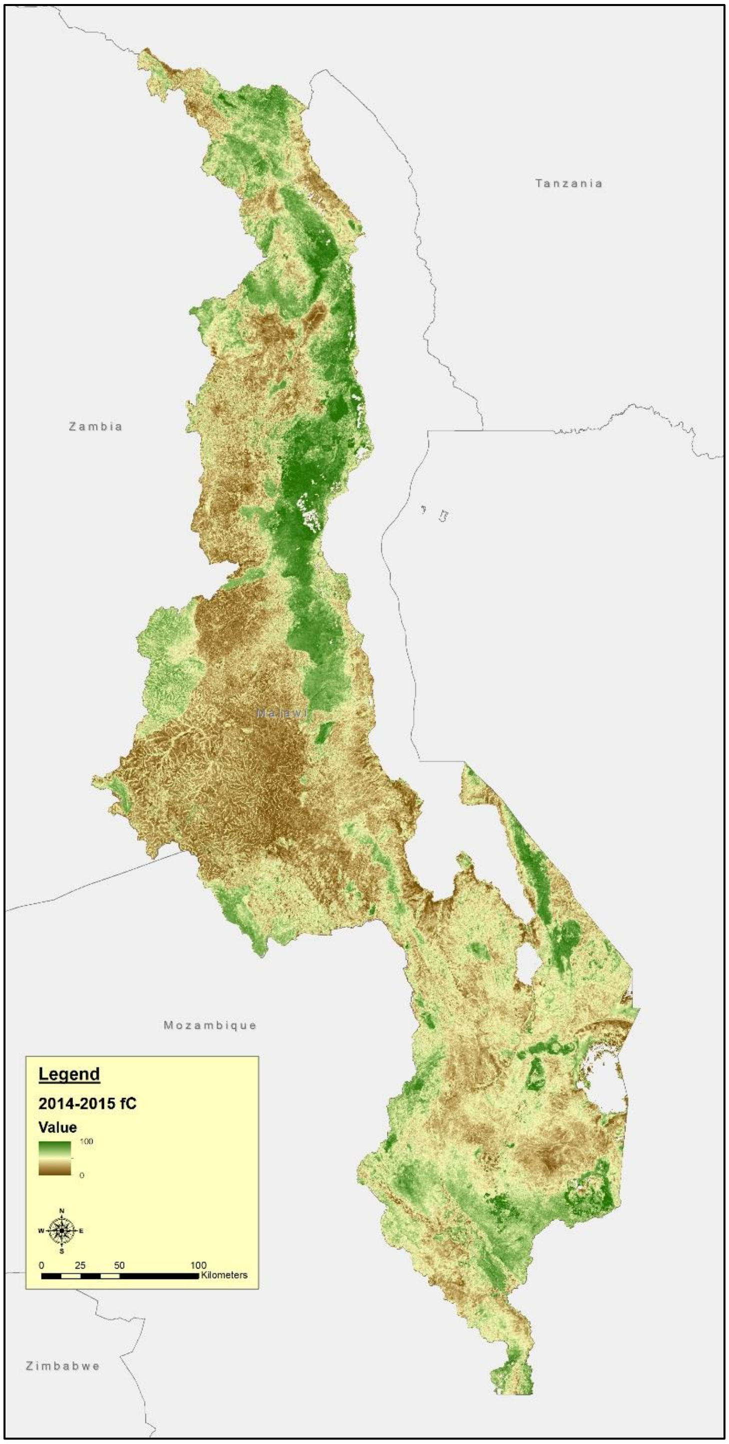

Figure 11: The national *f*C dataset for the time period 2014-2015.

IV. Accuracy Assessment Using High-Resolution Imagery

High resolution satellite imagery (spatial resolution of 1 m or less) was purchased from Apollo Mapping to support an accuracy assessment and validation of the *f*C results. A search was performed for imagery with minimal cloud cover and ideal nadir conditions for coverage of the 3 study areas. After searching, three images were selected for purchase that covered the forest reserves Perekezi and Liwonde. These images were also selected based on their close temporal proximity to the Landsat imagery used in the early dry season analysis. The Perekezi scene was a GeoEye-1 50 cm pan-sharpened orthorectified 4-band image acquired on May 31, 2014. Parts of Liwonde were covered by two images covering the east and west portions of the protected forest area. The west scene was a WorldView-3 50 cm pan-sharpened orthorectified 4-band image acquired on May 7, 2015, and the east scene was a WorldView-2 50 cm pan-sharpened orthorectified 4-band image acquired on April 28, 2015.

Image Target	Sensor	Acquisition Date
Perekezi	GeoEye-1	5/31/2014
Liwonde (west)	WorldView-3	5/7/2015
Liwonde (east)	WorldView-2	4/28/2015

Table 5: High resolution satellite images used for the purpose of accuracy assessment of the fractional cover product

High resolution imagery was obtained to create a classification of forest cover as a GIS layer which could be used as a reference layer surrogate to ground validation (i.e. ground truth). The reasoning behind this is that the high-resolution data represents an unmixed land cover image depicting spatial objects, usually individual trees, without mixed spectral responses. Thus, high resolution data directly portray what the models using medium-resolution Landsat imagery predict. However, classification of high-resolution imagery using traditional statistical classifiers is rather difficult because the sensor detects a much higher degree of spatial and spectral variation within each land cover type. Therefore, it is necessary to introduce other decision factors or to altogether reduce the spectral variation to avoid over-abundant “noise” in the classified product. In high-resolution imagery, the spatial distribution of pixels can be combined with the spectral characteristics of pixels to aid in developing contiguous groups of land cover classes in what is known as object-based classification. Alternatively, unsupervised classification can be used to first partition the multispectral image into a pre-determined number of classes based on the spectral characteristics of the image. Then, these classes can be manually combined into the desired final classified product. Accuracy assessment was performed on the final classified product to determine the validity for further use.

Classification and accuracy assessment of high-resolution imagery was performed using ERDAS Imagine. For this workflow, the Advanced RGB clustering tool was used to first convert the DNs into a thematic layer of several hundred classes based on their spectral values. These classes were then grouped together manually by using the Grouping Tool to recode their class values to values corresponding to either vegetation or non-vegetation. The Neighborhood Majority Function with a 3x3 moving window size was applied to the original classified products to remove noise. The Accuracy Assessment tool was used to generate 100 randomly placed reference points. The original high-resolution images with the false-color near-infrared band combination were then used as reference layers to code each sample point as vegetation, non-vegetation, or background. These reference classes corresponded to the classes present in the high-resolution classified image. The final overall accuracy was 79%, 86%, and 89% for the Perekezi GeoEye-1 image, the Liwonde Worldview-3 image, and Liwonde Wordlview-3 image respectively. Based on the Kappa Statistic, the level of agreement for the classification is considered moderate for the Perekezi scene and substantial for the two Liwonde scenes (Landis and Koch 1977).

Confusion Matrix – Perekezi GeoEye-1 Image				
	Reference Data			
Classified Data	**Other**	**Bare Soil**	**Vegetation**	**Row Total**
Other	2	0	0	2
Bare Soil	0	33	11	44
Vegetation	0	10	44	54
Column Total	**2**	**43**	**55**	**100**

Table 6: The confusion matrix generated for the Perekezi GeoEye-1 high resolution vegetation/non-vegetation thematic layer.

Accuracy Totals – Perekezi GeoEye-1 Image					
Class Name	**Reference Totals**	**Classified Totals**	**Number Correct**	**Producers Accuracy**	**Users Accuracy**
Other	2	2	2	---	---
Bare Soil	43	44	33	76.74%	75.00%
Vegetation	55	54	44	80.00%	81.48%
Totals	100	100	79		
Overall Classification Accuracy = 79.00%					

Table 7: Accuracy totals for the Perekezi GeoEye-1 high resolution vegetation/non-vegetation thematic layer.

Kappa (K^) Statistics – Perekezi GeoEye-1 Image	
Overall Kappa Statistics = 0.5910	
Conditional Kappa for each Category	
Class Name	**Kappa**
Other	1
Bare Soil	0.5614
Vegetation	0.5885

Table 8: Conditional kappa statistics for the individual classes, as well as the overall kappa statistic for the Perekezi GeoEye-1 classification.

Confusion Matrix – Liwonde Worldview-3 Image				
	Reference Data			
Classified Data	**Other**	**Bare Soil**	**Vegetation**	**Row Total**
Other	3	0	0	3
Bare Soil	0	38	1	39
Vegetation	0	13	45	58
Column Total	3	51	46	100

Table 9 : The confusion matrix generated for the Liwonde Worldview-3 high resolution vegetation/non-vegetation thematic layer.

Accuracy Totals – Liwonde Worldview-3 Image					
Class Name	**Reference Totals**	**Classified Totals**	**Number Correct**	**Producers Accuracy**	**Users Accuracy**
Other	3	3	3	---	---
Bare Soil	51	39	38	74.51%	97.44%
Vegetation	46	58	45	97.83%	77.59%
Totals	100	100	86		
Overall Classification Accuracy = 86.00%					

Table 10*:* Accuracy totals for the Liwonde Worldview-3 high resolution vegetation/non-vegetation thematic layer.

Kappa (K^) Statistics – Liwonde Worldview-3 Image	
Overall Kappa Statistics = 0.7375	
Conditional Kappa for each Category	
Class Name	**Kappa**
Other	1
Bare Soil	0.9477
Vegetation	0.5849

Table 11: Conditional kappa statistics for the individual classes, as well as the overall kappa statistic for the Liwonde Worldview-3 classification.

Confusion Matrix - Liwonde Worldview-2 Image				
	Reference Data			
Classified Data	**Other**	**Bare Soil**	**Vegetation**	**Row Total**
Other	1	0	0	1
Bare Soil	0	50	11	61
Vegetation	0	0	38	38
Column Total	1	50	49	100

Table 12: The confusion matrix generated for the Liwonde Worldview-2 high resolution vegetation/non-vegetation thematic layer.

Accuracy Totals - Liwonde Worldview-2 Image					
Class Name	**Reference Totals**	**Classified Totals**	**Number Correct**	**Producers Accuracy**	**Users Accuracy**
Other	1	1	1	---	---
Bare Soil	50	61	50	100.00%	81.97%
Vegetation	49	38	38	77.55%	100.00%
Totals	100	100	89		
Overall Classification Accuracy = 89.00%					

Table 13: Accuracy totals for the Liwonde Worldview-2 high resolution vegetation/non-vegetation thematic layer.

Kappa (K^) Statistics – Liwonde Worldview-2 Image	
Overall Kappa Statistics = 0.7838	
Conditional Kappa for each Category	
Class Name	**Kappa**
Other	1.00
Non-Vegetation	0.6393
Vegetation	1.00

Table 14: Conditional kappa statistics for the individual classes, as well as the overall kappa statistic for the Liwonde Worldview-2 classification.

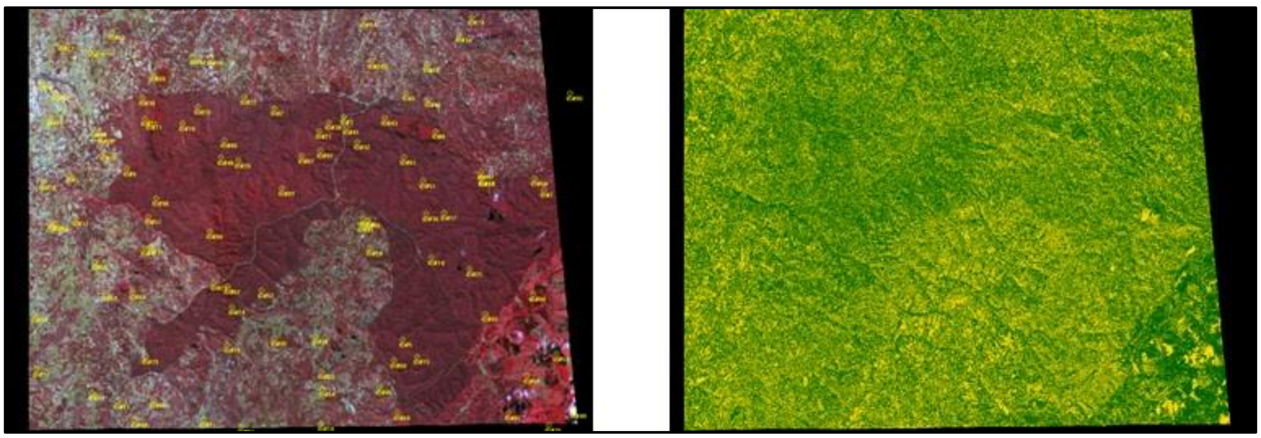

Figure 12: Perekezi GeoEye-1 Imagery. The multispectral image is on the left with the random sample points overlaid. The thematic vegetation/non-vegetation image is on the right.

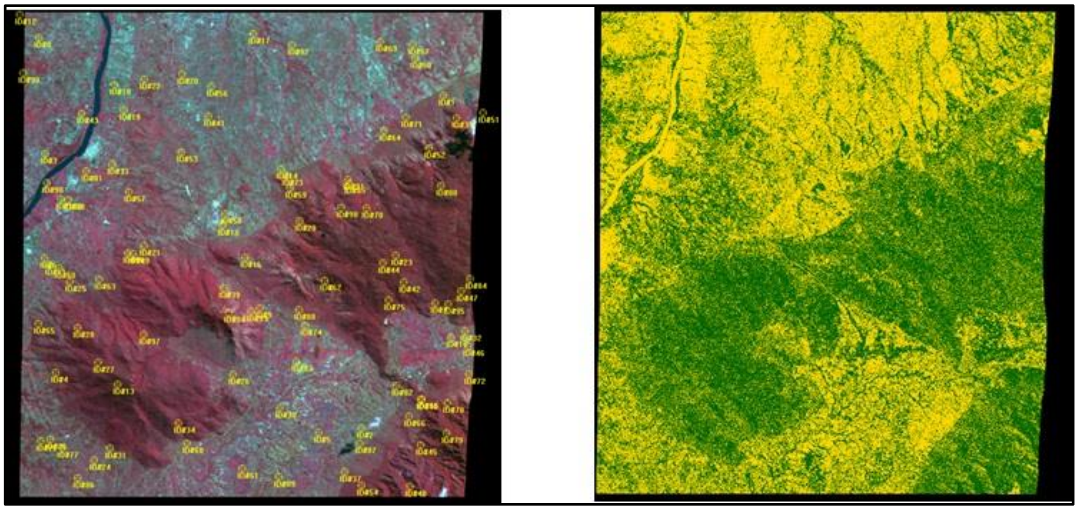

Figure 13: Liwonde Worldview-3 Imagery. The multispectral image is on the left with the random sample points overlaid. The thematic vegetation/non-vegetation image is on the right.

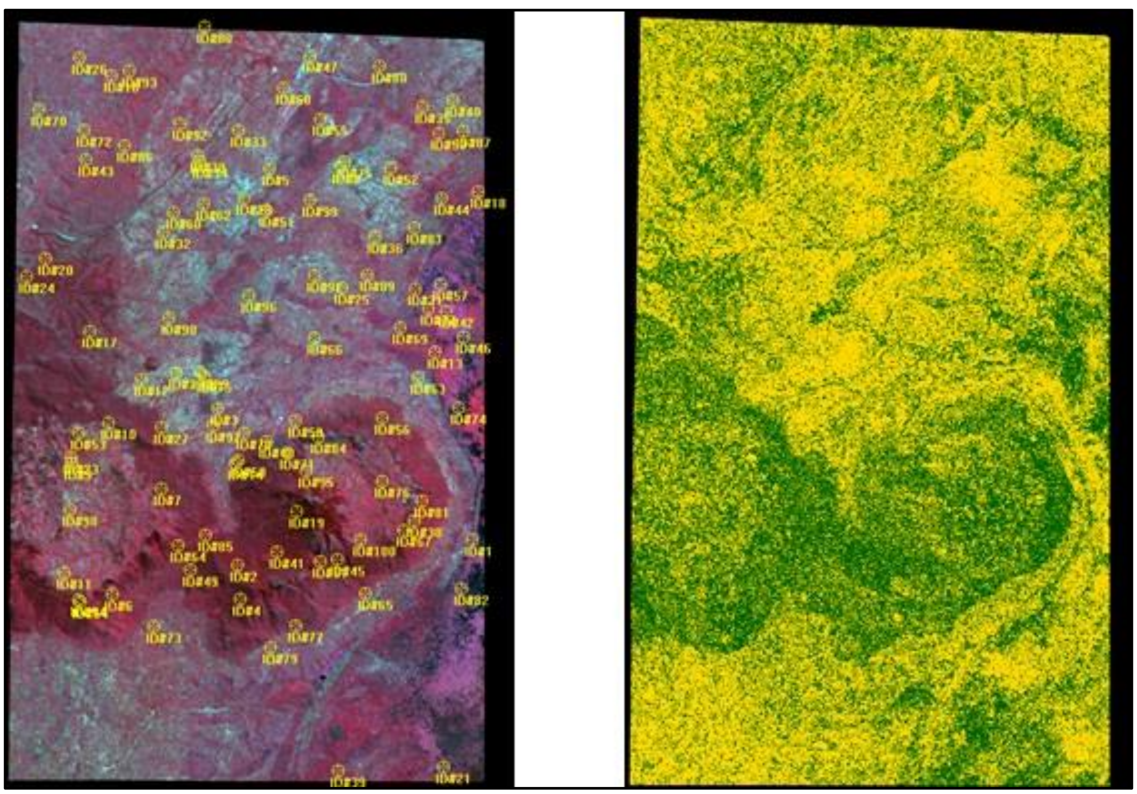

Figure 14: Liwonde Worldview-2 Imagery. The multispectral image is on the left with the random sample points overlaid. The thematic vegetation/non-vegetation image is on the right.

V. Accuracy Assessment of the Landsat-based *f*C Product

All GIS-related operations for this purpose were executed using ArcMap with the Spatial Analysis extension enabled. Determining the accuracy of the fractional cover product was carried out using the previously created high-resolution vegetation/non-vegetation classification map. This accuracy assessment was therefore done for the study areas of Perekezi and Liwonde due to the high-resolution imagery purchased for those sites. First, subsets of the study areas were generated from the national fractional cover dataset early dry season time period 2014-2015, which matched the high-resolution imagery acquisition dates and phenology most closely.

To relate 30 meter Landsat-derived fractional cover to the high-resolution 0.5 meter vegetation/non-vegetation classification, it was necessary to generate a standardized sampling grid. It was first decided to sample the fractional cover value for a randomly generated selection of 100 Landsat pixels. The extent of the high-resolution image area was digitized, and a grid of 30x30 meter squares was generated in this extent, along with the center point for each grid cell. The generated grid was edited so that it aligned with the extent of the Landsat pixels. A random selection of 100 center points was made. The center points were utilized to extract the value of *f*C at each Landsat pixel. The intersecting square polygons from the sampling grid were extracted for each of the 100 points as well and saved as a new polygon shapefile resulting in 100 square polygons. The result was a quantity of 100 center points and 100 square cells aligned with the Landsat fractional cover grid cells.

The utility of these two separate shapefiles is as follows: The point shapefile was used to extract the Landsat fractional cover value for each pixel that was intersected by a point feature, and then those values were entered into the attribute table of the point shapefile so that each row now had a corresponding fractional cover value. The point features were then related to the square cell polygon features using a spatial join, so that each row of the point attribute table had a corresponding square cell ID. Therefore, the points could then be grouped together within the attribute table based on the ID from each of the 100 corresponding square cells.

The square cell polygon shapefile was used to calculate the high-resolution fractional cover. This was performed by tabulating pixel counts by area. For each square cell, the number of pixels from each class of the high-resolution thematic image was counted and sorted based on class value. The fractional cover was then calculated for each cell as the sum of vegetation class pixels divided by the sum of all pixels per cell and multiplied by 100. The results of the tabulation were then joined to the attribute table of the point shapefile based on the square cell polygon ID field. These results were copied into a comma separated values (.csv) file and opened in R for statistical analysis (R Development Core Team 2008). The Landsat fractional cover could then be compared to the high-resolution fractional cover based on the ID of the square cell polygon.

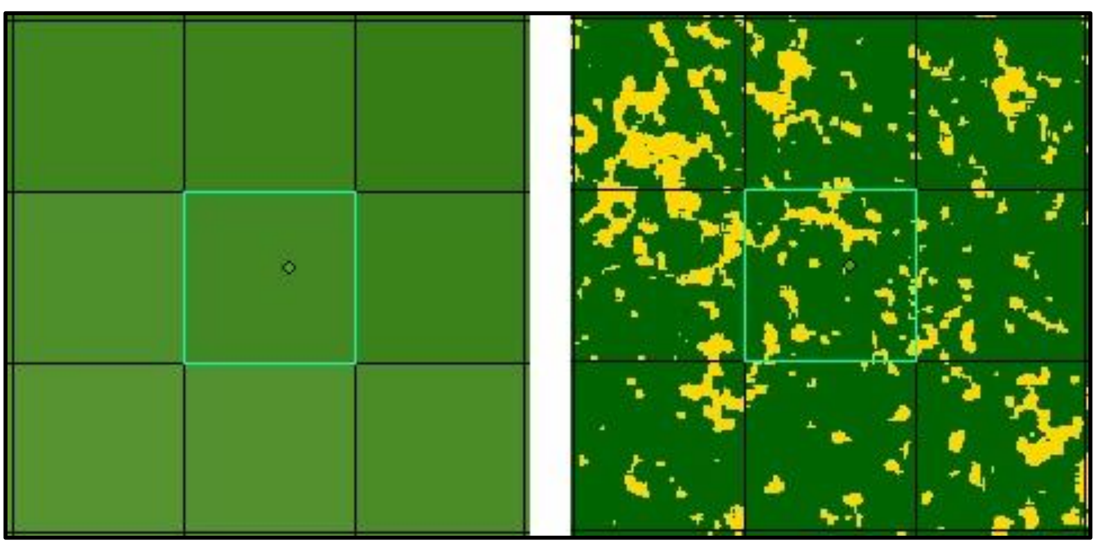

Figure 15: Comparison of the same spatial area shown in both the 30m fC product derived from Landsat data (left image) and the 0.5m thematic classification of vegetation and non-vegetation (right image).

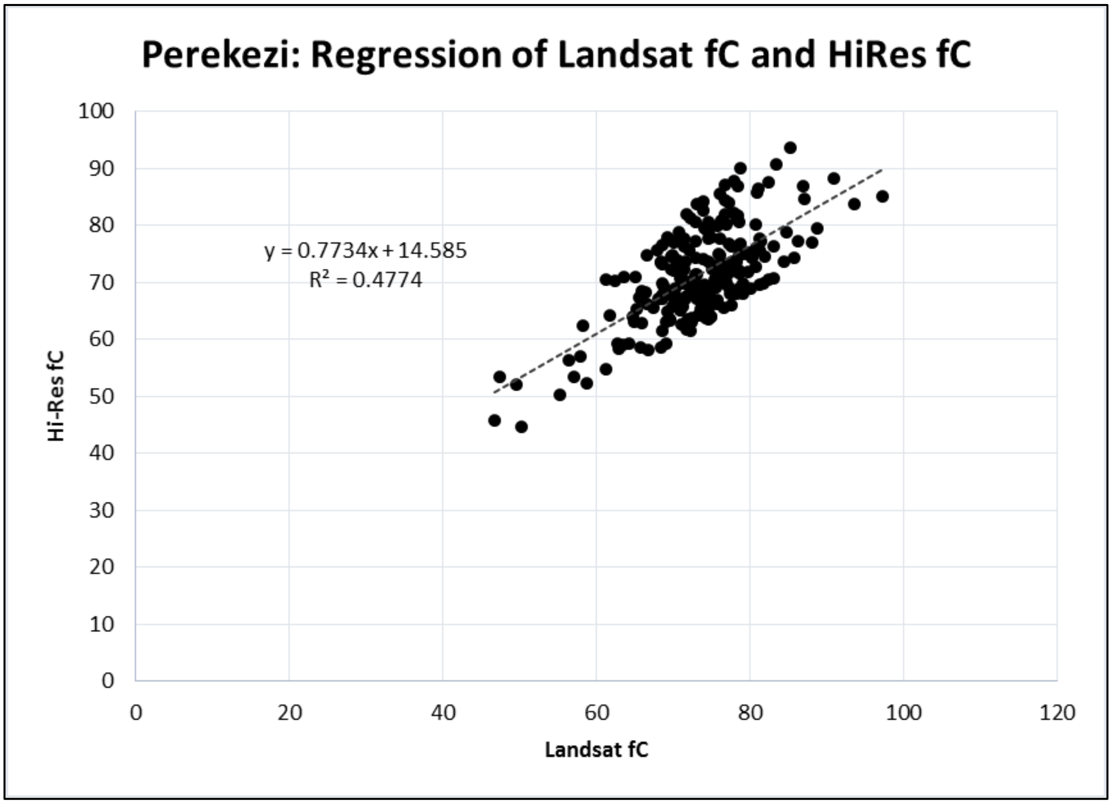

Figure 16: Perekezi regression of Landsat *f*C and HiRes *f*C. Simple linear regression plot between the Landsat *f*C (independent variable) and the hi-resolution *f*C (dependent variable) using the Perekezi Geoeye-1 imagery.

Perekezi SLR Results	
	Dependent variable: **Hi-Res *f*C**
Landsat fC	0.7734*** (0.7734)
Constant	14.585*** (4.050)
Observations	220
R^2	0.477
Adjusted R^2	0.475
Residual Std. Error	5.927 (df = 219)
F Statistic	199.137*** (df=1; 219)
Note:	*p<0.1; **p<0.05; ***p<0.01

Table 15: Perekezi SLR results. Simple linear regression results from the comparison of the Landsat derived *f*C (the independent variable) and the high resolution GeoEye-1 *f*C (the dependent variable).

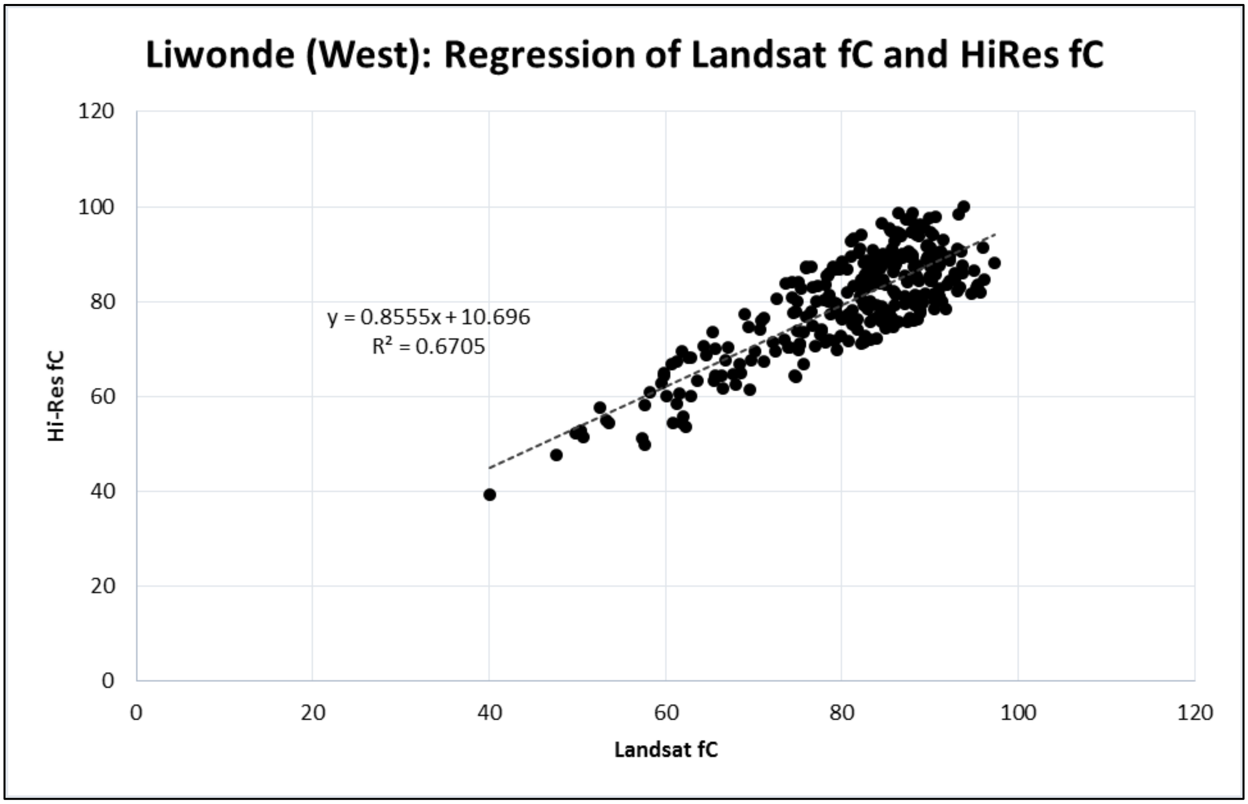

Figure 17: Liwonde (West) regression of Landsat *f*C and HiRes *f*C. Simple linear regression plot between the Landsat *f*C (independent variable) and the hi-resolution *f*C (dependent variable) using the Liwonde Worldview-3 imagery.

Liwonde (West) SLR Results	
	Dependent variable: **Hi-Res *f*C**
Landsat fC	0.8555*** (0.0353)
Constant	10.696***(2.870)
Observations	290
R^2	0.670
Adjusted R^2	0.669
Residual Std. Error	6.273 (df = 289)
F Statistic	588.049*** (df=1; 289)
Note:	*p<0.1; **p<0.05; ***p<0.01

Table 16: Liwonde (West) SLR results. Simple linear regression results from the comparison of the Landsat derived *f*C (the independent variable) and the high resolution Worldview-3 *f*C (the dependent variable).

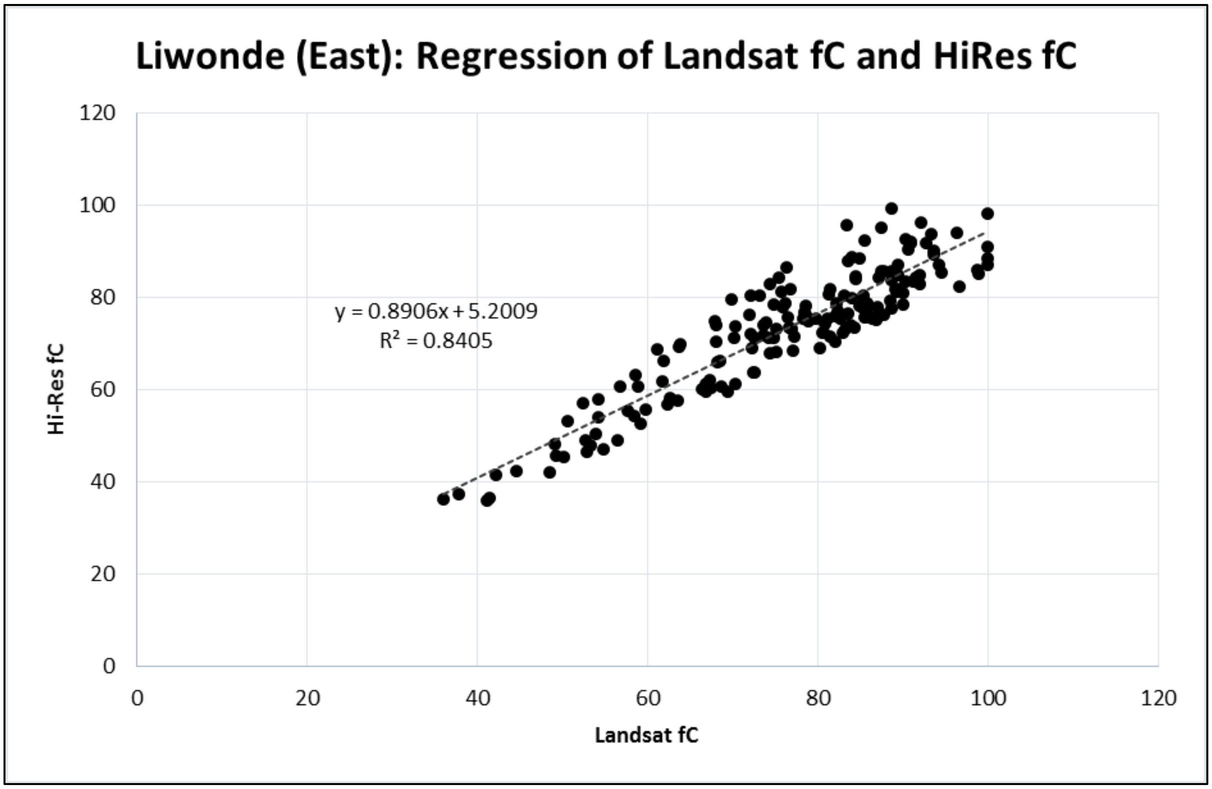

Figure 18: Liwonde (east) regression of Landsat *f*C and HiRes *f*C. Simple linear regression plot between the Landsat *f*C (independent variable) and the hi-resolution *f*C (dependent variable) using the Liwonde Worldview-2 imagery.

Liwonde (East) SLR Results	
	Dependent variable: **Hi-Res *f*C**
Landsat fC	0.8906*** (0.0303)
Constant	5.2009***(2.3503)
Observations	165
R^2	0.8405
Adjusted R^2	0.8340
Residual Std. Error	5.572 (df = 164)
F Statistic	864.485*** (df=1; 164)
Note:	*p<0.1; **p<0.05; ***p<0.01

Table 17: Liwonde (East) SLR results. Simple linear regression results from the comparison of the Landsat derived fC (the independent variable) and the high-resolution Worldview-2 fC (the dependent variable).

VI. Change Detection Algorithm

The usefulness of time series satellite imagery is that it provides measurements which directly record how a given landscape has been altered over time—both by anthropogenic and natural forces. Multispectral imagery such as Landsat contains a large amount of information that is difficult to quantify in n-dimensions where n is the number of bands present. Hence, classification techniques can be used to quantify targeted land cover types, or as is used in this study, vegetation indices and fractional cover analysis can be used to directly measure biophysical characteristics of vegetation. This can then be used to measure changes in vegetation such as Miombo woodlands over time.

A graphical model was built in ERDAS Imagine to process change detection between two spatially related periods of time using the national *f*C datasets as inputs. The change model had 3 main functions. A minimum change detection threshold of 10 was used as a filter because it was assumed that any reduction in *f*C of less than this was both negligible and likely temporary.

The first function in the model calculated the difference between the earlier date *f*C and the later date *f*C ($fC_2 - fC_1$) so that a decrease in *f*C across time yielded a negative value. A conditional statement was included in this difference function to ignore any results that were greater than or equal to 0, which means any positive or null changes in *f*C were ignored. In other words, only decreases in vegetation are being examined in this study. Two simultaneous functions were also applied to the individual *f*C inputs. These functions binned the *f*C datasets into 6 categories based on the actual *f*C values. The binned *f*C datasets were used as inputs along with the results of the differencing function into the last function of the model. This function compared the binned classes of fC_1 and fC_2 to determine if a pixel was either degradation or deforestation. The differencing results were used to only accept change that was at least a magnitude of 10 or greater, meaning that minimum decrease of 10 in *f*C was enforced here. Deforestation and degradation were categorized based on how a pixel changed between *f*C classes, and also whether or not that pixel met the minimum change requirement. This minimum requirement was enforced for both degradation and deforestation.

A land cover dataset was used to mask out non-forest areas. This meant that changes in *f*C would only be examined in areas designated broadly as protected forest areas.

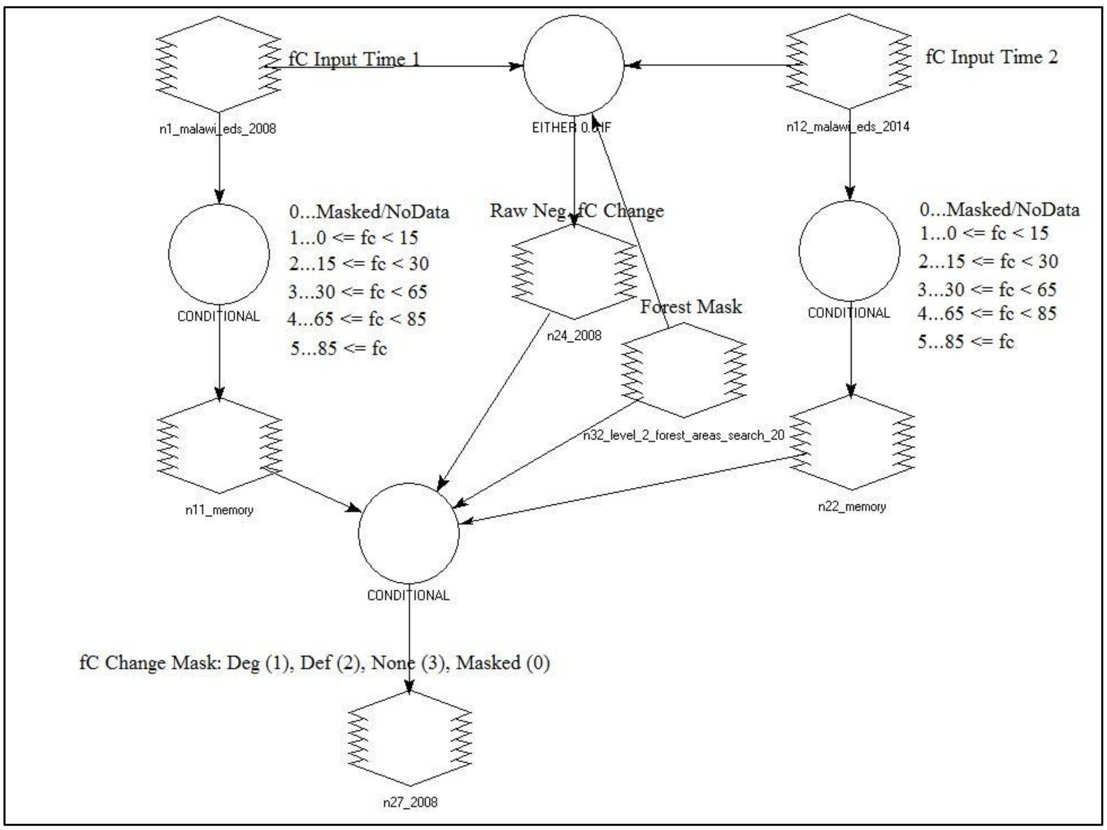

Figure 19: ERDAS graphical model used to carry out the change detection between two *f*C datasets.

VII: Change Detection Algorithm Results

Between the epochs of 2000 and 2009 a total of 248,007 Ha of forest land was degraded, but remained forest, while 16,202 Ha of forest land was deforested based on the comparison of fC values for the two datasets corresponding to these dates. Between the years of 2010 and 2015 a total of 254,257 Ha of forest land was degraded and 9,037 Ha of forest land was deforested based on the comparison of fC values for the two datasets corresponding to these dates.

For the time period of 2010 to 2015, of the 254,257 Ha of forest that was degraded, 36,159 Ha was in forest that were further degraded from forest degraded in 2000-2009 was further degraded. Also, between 2010 and 2015, of the 9,037 Ha of deforested land, 5,547 Ha of that occurred on forested land that was previously degraded between 2002 and 2010. Likewise, between 2010 and 2015 218,097 Ha of the 254,257 Ha of degradation occurred on forest land that had not been previously degraded. Similarly, 3,490 Ha of the total 9,037 Ha that were deforested between 2010 and 2015 occurred on land that was not previously degraded between 2002 and 2010.

The total area of protected forests in Malawi, as determined from the available land-cover dataset, is 2,399,381 Ha. Between 2002 and 2010, 10.34% of protected forests were degraded and 0.68% of protected forests were deforested. Between 2010 and 2015, 10.59% of protected forests were degraded and 0.38% of protected forests were deforested.

Figure 20 shows the mapped results of the change detection algorithm. Three insets are provided in addition to the national scale map; each inset shows a protected forest area. Two of these protected forest areas were also used for the validation of the *f*C product via the use of high-resolution imagery. Inset A shows Perekezi forest reserve, inset B shows Ntchisi forest reserve, and inset C shows Liwonde forest reserve. Areas of degradation for the 2 change periods are clearly visible in each reserve. A number of previously identified drivers is likely responsible, however there may be a few caveats to these results. Primarily, orchards were not considered in the change algorithm. All land within the protected forest reserves was considered to be forest. However, orchards are present for example in southeastern Perekezi, and it is possible that these could contribute to false positives in the change results.

2002 to 2010 Change Results		
Change Type	**Area (ha)**	**% of Total Forest Area**
Degradation	248,007	10.34 %
Deforestation	16,202	0.68 %
Total Forest Area	2,399,381	11.01 %

Table 18: 2002 to 2010 change results. Area in hectares of each change category for the time period from 2002 to 2010. The percent of total forest area for each change category is also shown.

2010 to 2015 Change Results		
Change Type	**Area (ha)**	**% of Total Forest Area**
Degradation	254,257	10.59 %
Deforestation	9,037	0.38 %
Total Forest Area	2,399,381	10.97 %

Table 19: 2010 to 2015 change results. Area in hectares of each change category for the time period from 2010 to 2015. The percent of total forest area for each change category is also shown.

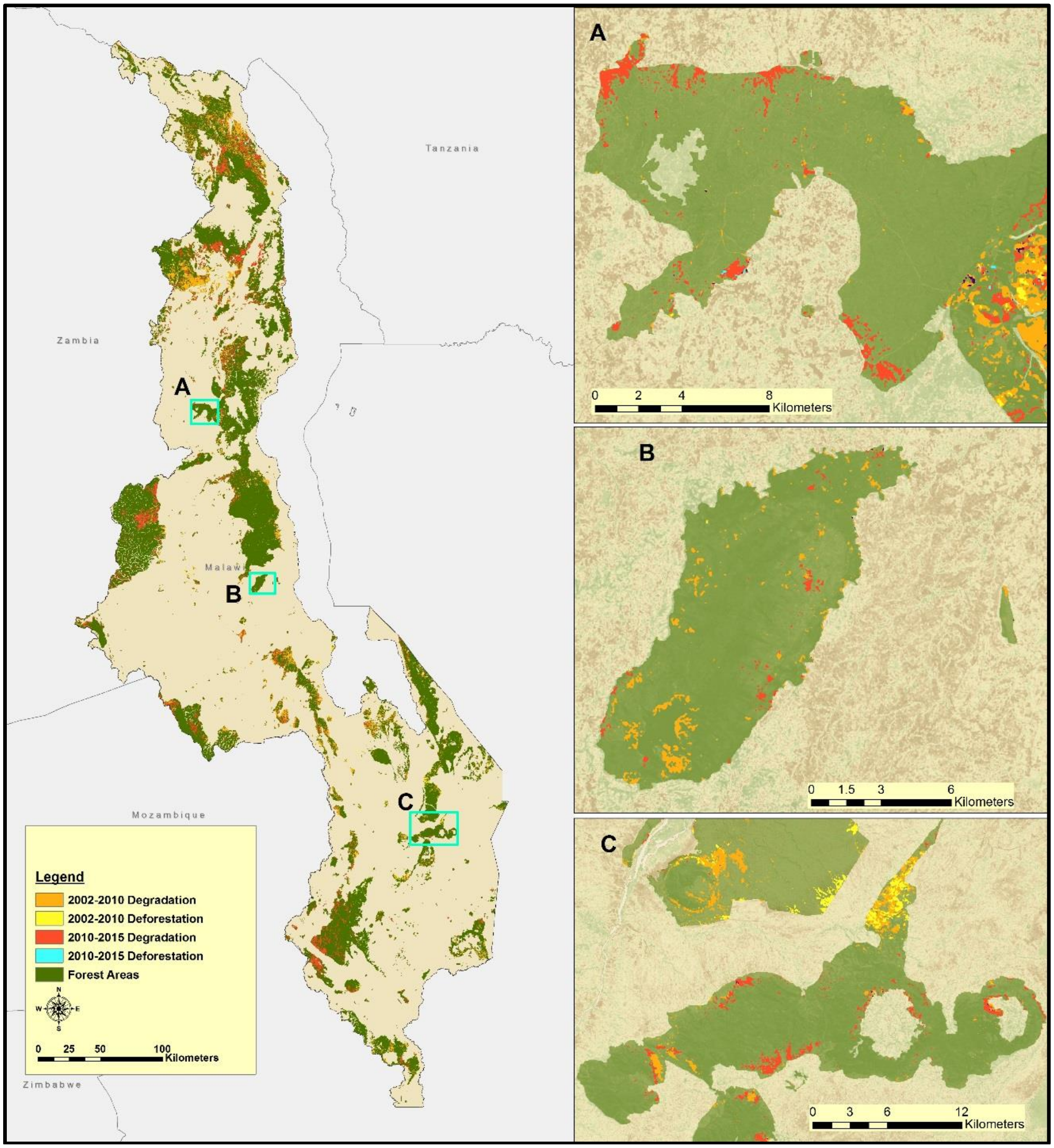

Figure 20: The change algorithm results are shown here for the two lengths of time 2002-2010 and 2010-2015. The types of change that occurred in each period are color coded. Inset A shows the detail area around Perekezi Forest Reserve which includes a western portion of the South Viphya Forest Reserve. Inset B shows the detailed area around Ntchisi Forest Reserve. Inset C shows the detailed area around Liwonde Forest Reserve, which also includes the southern portion of Liwonde National Park and the northern portion of the Zomba-Malosa Forest. All protected forests are indicated by the green areas on the main map and insets.

VIII: Validation of Change Detection Algorithm Results

The accuracy assessment for the results of the change algorithm was carried out by calculating a confusion matrix from a set of stratified random sample points. The GeoEye-1 image acquired for the area covering the Perekezi forest reserve was used as a reference layer to confirm the presence of the classified change types. For this scenario, 100 stratified random points were generated and the parameter for a minimum number of points per class was set to 10 to ensure deforestation was sampled due to its relatively smaller area compared to the other two change classes. Google Earth imagery was also used as a reference for earlier time period high-resolution imagery by spatially-linking an ERDAS viewer to the Google Earth user interface. However, earlier time period high-resolution imagery was not available for most sample points so inferences had to be made as to the nature and time period for areas of forest that were cleared or degraded in the purchased high resolution imagery due to a lack of reference. If a sample point fell within an open agricultural field in the more recent high resolution image, then Google Earth was referenced to confirm whether or not that clearing was made within the time period measured by the Landsat imagery. If the clearing was made prior to the Landsat imagery acquisition, then it should be considered an area of no change. The Landsat multispectral mosaic images from the two time periods were used as a reference as well to observe the source of any potentially detected change directly. The purchased high resolution imagery was however used as the primary deciding factor in assigning reference classes to the sample points. If no earlier reference point was available, then areas that were obviously cleared for agriculture or that had sparse canopy cover and proximity to agriculture or settlements were assigned degradation and deforestation values depending on the openness of the land where the sample points were located. This was suitable for testing the accuracy of the Landsat-derived change detection because it was shown earlier that the high-resolution classified percent vegetation cover correlated fairly well to the Landsat fractional cover.

Confusion Matrix for Change Detection				
	Reference			
Classified	**No Change**	**Degradation**	**Deforestation**	**Row Total**
No Change	46	7	1	**54**
Degradation	4	21	3	**28**
Deforestation	1	1	16	**18**
Column Total	**51**	**29**	**20**	**100**

Table 20: Confusion matrix for change detection. The confusion matrix that was created as part of the accuracy assessment of the change algorithm. The rows represent the classified change algorithm product, and the columns represent the ground-truth reference totals. The diagonal of the table represents correctly labeled change classes.

Accuracy Totals for Change Detection					
Class Name	**Reference Totals**	**Classified Totals**	**Number Correct**	**Producers Accuracy**	**Users Accuracy**
No Change	51	54	46	90.2%	85.2%
Degradation	29	28	21	72.41%	75%
Deforestation	20	18	16	80.0%	88.89%
Totals	100	100	83		
Overall Classification Accuracy = 83%					

Table 21: Accuracy totals for change detection. The accuracy totals are shown for the producer's, user's, and overall accuracies.

Kappa (K^) Statistics for Change Detection	
Overall Kappa Statistics = 0.7201	
Conditional Kappa for each Category	
Class Name	**Kappa**
No Change	0.6977
Degradation	0.6479
Deforestation	0.8611

Table 22: Kappa (K^) statistics for change detection. Conditional kappa values calculated for each individual class as well as the kappa value for the overall classification.

Tables 20-22 show the results of the accuracy assessment. The confusion matrix was built first to determine the number of correctly or incorrectly assigned change categories (table 20). From this, the producer's, user's and overall accuracies were calculated (table 21). Finally, these accuracies were used to calculate the overall kappa statistic (table 22). The overall kappa statistic equaled 0.7201, which is a substantial result indicating the success of the change algorithm for detecting degradation and deforestation (Landis and Koch 1977).

IX: Discussion and Conclusion

Three Malawi national-scale Landsat multispectral mosaics representing unique epochs of time were generated. A continuous fields fractional cover of vegetation was calculated from each of these Landsat mosaics. A technique was successfully demonstrated which uses the *f*C product to detect changes in vegetation cover over time. Negative change in vegetation cover within protected forest lands represents forest degradation from one epoch to the next. This type of change detection is particularly important for the forestry sector due to the proliferation of both high and low impact forest use. It is necessary for REDD+ efforts in Malawi to be able to accurately quantify current levels of forest degradation to generate reference emission levels. The *f*C products allowed for a robust and accurate method of directly locating areas where degradation and deforestation have occurred. Therefore, it is a recommendation that the technique demonstrated here be implemented as part of a measurement, reporting, and verification (MRV) tool, which is a requirement of UNFCCC and IPCCC for REDD+ in Malawi and other countries.

The actual quantification of biomass removal may be estimated based on the *f*C change results, but it should be verified and recalibrated with extensive on-the-ground measurements. Other forms of remote sensing such as LiDAR and high-resolution satellite imagery may provide a means of further calibrating the Landsat-derived fractional cover and allow for a more accurate biomass measurement. Mapping the locations of degradation and deforestation with Landsat imagery as shown in this study is an effective means to direct REDD+ mitigation strategies and can also help to inform afforestation activities for Malawi's protected forests. These change products can also be used to develop remote sensing-based activity data to assist with calculating reference emission levels for REDD+.

Both degradation and deforestation were observed across the entire national extent of Malawi. Based on the analysis of Landsat data, the extent of these areas was quantified. Similarly, the use of remote sensing data allowed for locating the hotspots of deforestation and forest degradation across the country of Malawi. It is not surprising that these areas coincide with locations of protected forest areas. This is likely due to the fact that much of the country has already been extensively deforested. The remaining areas of Miombo woodland are therefore primarily located within these protected forests. The protected forest status may prevent land cover change from forest to agriculture which prevents deforestation. However, forest degradation may still occur because these remaining woodlands represent a source of fuel wood and other wood-based resources, which is driven by the extensive poverty and lack of alternative energy resources for the majority of Malawians.

Between 2002 and 2010 248,007 Ha of Miombo woodlands were degraded, and between 2010 and 2015 254,257 Ha of Miombo woodlands were degraded based on the analysis presented here. Deforestation of Miombo woodlands between 2002 and 2010 totaled 16,202 Ha and between 2010 and 2015 totaled 9,037 Ha. This supports the conclusion that much of Malawi is already deforested, and that the remaining protected forests are still susceptible to exploitation that results in forest degradation.

One caveat to the national *f*C datasets is the use of static endmembers. Because the *f*C algorithm works by taking in a single endmember value for each of the two cover-types, it may not be the most accurate depiction of vegetation cover across a large area (Johnson, Tateishi, and Kobayashi 2012). This is due to the variation in land cover types, predominant forms of vegetation, and distribution of micro-climates across a large region such as Malawi. Despite atmospheric corrections and image normalization, differences may still exist between adjacent and gap-fill Landsat scenes which could necessitate individual scene-specific endmembers. This could mean that scene-specific endmembers might be more effective for measuring *f*C at the scale of individual forest reserves. Spatial interpolation of endmembers is one theoretical solution to this problem (Johnson, Tateishi, and Kobayashi 2012). More work should be done on which type of spatial interpolation is more effective, and how accurately the endmembers of target land cover types can be modeled in such a way as to generate a more meaningful *f*C over a large area. However, despite this caveat, the technique demonstrated of using a two-endmember SMA was sufficient for accurately measuring the presence of vegetation across the landscape at a 30-meter resolution.

There is potential for more remote sensing work to be done in Malawi. By adding more dates to the analysis, a higher temporal resolution could be obtained. This would allow for a clearer picture to emerge which indicates when and where Miombo woodlands are being degraded. This can certainly help to inform mitigation and outreach efforts with local communities. Furthermore, the ability to quantify biomass directly from Landsat satellite observations would allow for a robust and efficient method to develop activity data necessary for developing REDD+ in Malawi.

A technique for using *f*C to map change in open canopy Miombo woodlands has been demonstrated. Specific locations of degradation and deforestation within Malawi protected forest areas have been produced. The usefulness of the freely available Landsat data archive has also been demonstrated as a reliable and scientifically robust data source for generating vegetation cover maps. Activity data related to forest loss and degradation can be acquired by comparing *f*C across time to calculate delta *f*C values. These delta values have been shown in this study to be a promising method for estimating forest degradation in Malawi, and these methods have potential for reproducibility to develop activity data for other countries. These efforts have also assisted with the Malawi PERFORM project by providing actionable scientific data describing locations and magnitudes of Miombo degradation in Malawi. PERFORM is a capacity building project to assist Malawi with developing a framework to prepare for REDD+ and increase forest conservation. PERFORM was designed as a primary mechanism between the United States Government and Government of Malawi to promote lowering emissions via conservation and sustainable forestry practices.

BIBLIOGRAPHY

BIBLIOGRAPHY

Abbot, Joanne I. O., and Katherine Homewood. 1999. “A History of Change: Causes of Miombo Woodland Decline in a Protected Area in Malawi.” *Journal of Applied Ecology* 36 (3): 422–33.

Adams, John B., Donald E. Sabol, Valerie Kapos, Raimundo Almeida Filho, Dar A. Roberts, Milton O. Smith, and Alan R. Gillespie. 1995. “Classification of Multispectral Images Based on Fractions of Endmembers: Application to Land-Cover Change in the Brazilian Amazon.” *Remote Sensing of Environment* 52 (2): 137–54.

ArcGIS for Desktop (version 10.2.2). 2015. Redlands, CA: ESRI Inc.

Bonan, Gordon B. 2008. “Forests and Climate Change: Forcings, Feedbacks, and the Climate Benefits of Forests.” *Science* 320 (5882): 1444–49.

Broich, Mark, Matthew C. Hansen, Peter Potapov, Bernard Adusei, Erik Lindquist, and Stephen V. Stehman. 2011. “Time-Series Analysis of Multi-Resolution Optical Imagery for Quantifying Forest Cover Loss in Sumatra and Kalimantan, Indonesia.” *International Journal of Applied Earth Observation and Geoinformation* 13 (2): 277–91.

Broich, Mark, Matthew Hansen, Fred Stolle, Peter Potapov, Belinda Arunarwati Margono, and Bernard Adusei. 2011. “Remotely Sensed Forest Cover Loss Shows High Spatial and Temporal Variation across Sumatera and Kalimantan, Indonesia 2000–2008.” *Environmental Research Letters* 6 (1): 014010.

Brouwer, Inge D., Jan C. Hoorweg, and Marti J. van Liere. 1997. “When Households Run out of Fuel: Responses of Rural Households to Decreasing Fuelwood Availability, Ntcheu District, Malawi.” *World Development* 25 (2): 255–66.

Carlson, Toby, and David A. Ripley. 1997. “On the Relation between NDVI, Fractional Vegetation Cover, and Leaf Area Index.” *Remote Sensing of Environment* 62: 241–52.

Chander, Gyanesh, Brian L. Markham, and Dennis L. Helder. 2009. “Summary of Current Radiometric Calibration Coefficients for Landsat MSS, TM, ETM+, and EO-1 ALI Sensors.” *Remote Sensing of Environment* 113: 893–903.

Chavez Jr., Pat S. 1988. “An Improved Dark-Object Subtraction Technique for Atmospheric Scattering Correction of Multispectral Data.” *Remote Sensing of Environment* 24 (3): 459–79.

Chavez, Pat S. 1996. “Image-Based Atmospheric Corrections—revisited and Improved.” *Photogrammetric Engineering & Remote Sensing* 62 (9): 1025–36.

Chavula, Geoffrey, Patrick Brezonik, and Marvin Bauer. 2011. "Land Use and Land Cover Change (LULC) in the Lake Malawi Drainage Basin, 1982-2005." *International Journal of Geosciences* 02 (02): 172.

Chidumayo, Emmanuel, and Peter Frost. 1996. "Population Biology of Miombo Trees." In *The Miombo in Transition: Woodlands and Welfare in Africa*, edited by Bruce Campbell. Bogor, Indonesia: CIFOR.

Cochrane, M. A., and C. M. Souza. 1998. "Linear Mixture Model Classification of Burned Forests in the Eastern Amazon." *International Journal of Remote Sensing* 19 (17): 3433–40.

Corbera, Esteve, and Heike Schroeder. 2011. "Governing and Implementing REDD+." *Environmental Science & Policy*, Governing and Implementing REDD+, 14 (2): 89–99.

Desanker, PV, PGH Frost, CO Justice, and RJ Scholes. 1997. "The Miombo Network: Framework for a Terrestrial Transect Study of Land-Use and Land-Cover Change in the Miombo Ecosystems of Central Africa." IGBP Report 41. Stockholm, Sweden: The International Geosphere-Biosphere Program.

Elmore, Andrew J., Mustard, John F., Manning, Sara J., Lobell, David B. 2000. "Quantifying Vegetation Change in Semiarid Environments: Precision and Accuracy of Spectral Mixture Analysis and the Normalized Difference Vegetation Index." *Remote Sensing of Environment* 73 (1): 87-102

Elvidge, Christopher and Yuan, Ding & Weerackoon, R.D. and Lunetta, R.S.. 1995. "Relative Radiometric Normalization of Landsat Multispectral Scanner (MSS) Data Using an Automatic Scattergram-Controlled Regression." *Photogrammetric Engineering & Remote Sensing*. 61. 1255-1260.

ERDAS Imagine. 2014. Madison, AL: Intergraph Corporation.

Frost, Peter. 1996. "The Ecology of Miombo Woodlands." In *The Miombo in Transition: Woodlands and Welfare in Africa*, edited by Bruce Campbell. Bogor, Indonesia: CIFOR.

Goetz, Scott, and Ralph Dubaya. 2011. "Advances in Remote Sensing Technology and Implications for Measuring and Monitoring Forest Carbon Stocks and Change." *Carbon Management* 2 (3): 231–44.

Haack, Barry, Ron Mahabir, and John Kerkering. 2015. "Remote Sensing-Derived National Land Cover Land Use Maps: A Comparison for Malawi." *Geocarto International* 30 (3): 270–92.

Hansen, Matthew C., and Thomas R. Loveland. 2012. "A Review of Large Area Monitoring of Land Cover Change Using Landsat Data." *Landsat Legacy Special Issue* 122 (0): 66–74.

Hansen, Matthew C., David P. Roy, Erik Lindquist, Bernard Adusei, Christopher O. Justice, and Alice Altstatt. 2008. "A Method for Integrating MODIS and Landsat Data for Systematic Monitoring of Forest Cover and Change in the Congo Basin." *Earth Observations for Terrestrial Biodiversity and Ecosystems Special Issue* 112 (5): 2495–2513.

Hansen, Matthew C., Stephen V. Stehman, and Peter V. Potapov. 2010. "Quantification of Global Forest Cover Loss." *Proc Natl Acad Sci U S A* 107 (19): 8650–55.

Hansen, Matthew C., Stephen V. Stehman, Peter V. Potapov, Belinda Arunarwati, Fred Stolle, and Kyle Pittman. 2009. "Quantifying Changes in the Rates of Forest Clearing in Indonesia from 1990 to 2005 Using Remotely Sensed Data Sets." *Environmental Research Letters* 4: 12.

Hansen, Matthew C., Stephen V. Stehman, Peter V. Potapov, Thomas R. Loveland, John R. G. Townshend, Ruth S. DeFries, Kyle W. Pittman, et al. 2008. "Humid Tropical Forest Clearing from 2000 to 2005 Quantified by Using Multitemporal and Multiresolution Remotely Sensed Data." *Proceedings of the National Academy of Sciences* 105 (27): 9439–44.

Hansen, M. C., R. S. DeFries, J. R. G. Townshend, M. Carroll, C. Dimiceli, and R. A. Sohlberg. 2003. "Global Percent Tree Cover at a Spatial Resolution of 500 Meters: First Results of the MODIS Vegetation Continuous Fields Algorithm." *Earth Interactions* 7 (10): 1–15.

Houghton, JT, LG Meira Filho, B Lim, K Treanton, and I Mamaty. 1997. "Revised 1996 IPCC Guidelines for National Greenhouse Gas Inventories. v. 1: Greenhouse Gas Inventory Reporting Instructions.-v. 2: Greenhouse Gas Inventory Workbook.-v. 3: Greenhouse Gas Inventory Reference Manual."

Hudak, Andrew T., and Carol A. Wessman. 2000. "Deforestation in Mwanza District, Malawi, from 1981 to 1992, as Determined from Landsat MSS Imagery." *Applied Geography* 20 (2): 155–75.

Huete, A. R. 1988. "A Soil-Adjusted Vegetation Index (SAVI)." *Remote Sensing of Environment* 25 (3): 295–309.

IPCC. 1990. "Climate Change: The IPCC Scientific Assessment." IPCC First Assessment Report. Cambridge, Great Britain, New York, NY, USA and Melbourne Australia: IPCC.

IPCC. 2014a. *Climate Change 2014: Synthesis Report. Contribution of Working Groups I, II, and III to the Fifth Assessment Report of the Intergovernmental Panel on Climate Change*. Edited by Core Writing Team, R.K. Pachauri, and L.A. Meyer. Geneva, Switzerland: IPCC.

IPCC 2014b. “Summary for Policymakers.” In *Climate Change 2014: Impacts, Adaptation, and Vulnerability. Part A: Global and Sectoral Aspects. Contribution of Working Group II to the Fifth Assessment Report of the Intergovernmental Panel on Climate Change*, edited by C. B. Field, V. R. Barros, D. J. Dokken, K. J. Mach, M. D. Mastrandrea, T. E. Bilir, M. Chatterjee, et al., 1–32. Cambridge, United Kingdom, and New York, NY, USA: Cambridge University Press.

Irons, James R., John L. Dwyer, and Julia A. Barsi. 2012. “The next Landsat Satellite: The Landsat Data Continuity Mission.” *Remote Sensing of Environment*, Landsat Legacy Special Issue, 122 (July): 11–21.

Johnson, Brian, Ryutaro Tateishi, and Toshiyuki Kobayashi. 2012. “Remote Sensing of Fractional Green Vegetation Cover Using Spatially-Interpolated Endmembers.” *Remote Sensing* 4: 2619–34.

Keeling, Charles D., Robert B. Bacastow, Arnold E. Bainbridge, Carl A. Ekdahl, Peter R. Guenther, Lee S. Waterman, and John F. S. Chin. 1976. “Atmospheric Carbon Dioxide Variations at Mauna Loa Observatory, Hawaii.” *Tellus* 28 (6): 538–51.

Landis, J. Richard, and Gary G. Koch. 1977. “The Measurement of Observer Agreement for Categorical Data.” *Biometrics* 33 (1): 159–74.

Lillesand, Thomas, Ralph W Kiefer, and Jonathan Chipman. 2008. *Remote Sensing and Image Interpretation*. 6th ed. John Wiley & Sons.

MASDAP. 2013. “Malawi International Boundary.” Malawi Surveys Department. http://www.masdap.mw/layers/geonode%3Amwi_adm0.

Matricardi, E. A. T., D. L. Skole, M. A. Cochrane, M. Pedlowski, and W. Chomentowski. 2007. “Multi-temporal Assessment of Selective Logging in the Brazilian Amazon Using Landsat Data.” *International Journal of Remote Sensing* 28 (1): 63–82.

Matricardi, Eraldo A. T., David L. Skole, Marcos A. Pedlowski, Walter Chomentowski, and Luis Claudio Fernandes. 2010. “Assessment of Tropical Forest Degradation by Selective Logging and Fire Using Landsat Imagery.” *Remote Sensing of Environment* 114 (5): 1117–29.

Matricardi, Eraldo A. T., David L. Skole, Marcos A. Pedlowski & Walter Chomentowski (2013) Assessment of forest disturbances by selective logging and forest fires in the Brazilian Amazon using Landsat data, International Journal of Remote Sensing, 34:4, 1057-1086.

Navratil, Peter. 2013. “Land Cover Situation and Land-Use Change in the Districts of West Kalimantan and East Kalimantan, Indonesia: Assessment of District and Forest Management Unit Wide Historical Emission Levels.” Deutsche Gesellschaft für Internationale Zusammenarbeit (GIZ) GmbH FORCLIME Forests and Climate Change Programme.

Qi, J., A. Chehbouni, A. R. Huete, Y. H. Kerr, and S. Sorooshian. 1994. “A Modified Soil Adjusted Vegetation Index.” *Remote Sensing of Environment* 48 (2): 119–26.

Qi, J, R. C Marsett, M. S Moran, D. C Goodrich, P Heilman, Y. H Kerr, G Dedieu, A Chehbouni, and X. X Zhang. 2000. “Spatial and Temporal Dynamics of Vegetation in the San Pedro River Basin Area.” *Agricultural and Forest Meteorology* 105 (1–3): 55–68.

R Development Core Team. 2008. *R: A Language and Environment for Statistical Computing*. Vienna, Austria: R Foundation for Statistical Computing. http://www.R-project.org.

Ribeiro, Natasha, Aniceto Chaúque, Faruk Mamugy, and Micas Cumbana. 2012. *Remote Sensing of Biomass in the Miombo Woodlands of Southern Africa: Opportunities and Limitations for Research*. INTECH Open Access Publisher.

Roberts, D. A., M. Gardner, R. Church, S. Ustin, G. Scheer, and R. O. Green. 1998. “Mapping Chaparral in the Santa Monica Mountains Using Multiple Endmember Spectral Mixture Models.” *Remote Sensing of Environment* 65 (3): 267–79.

Skole, David, and Compton Tucker. 1993. “Tropical Deforestation and Habitat Fragmentation in the Amazon: Satellite Data from 1978 to 1988.” *Science* 260 (5116): 1905–10.

Smith, Pete, Mercedes Bustamante, Helal Ahammad, Harry Clark, Hongmin Dong, Elnour Abdalla Elsiddig, Helmut Haberl, et al. 2014. “Agriculture, Forestry and Other Land Use (AFOLU).” In *Climate Change 2014: Mitigation of Climate Change. Contribution of Working Group III to the Fifth Assessment Report of the Intergovernmental Panel on Climate Change*, edited by O. Edenhofer, R. Pichs-Madruga, Y. Sokona, E. Farahani, S. Kadner, K. Seyboth, A. Adler, et al. Cambridge, United Kingdom and New York, NY, USA.: Cambridge University Press.

UNFAO. 2010. *Global Forest Resources Assessment 2010: Main Report*. Food and Agriculture Organization of the United Nations.

UNFAO. 2015. “Forest Resource Assessment Working Paper 2015 Terms and Definitions.” Food and Agriculture Organization of the United Nations.

Tucker, C. J. 1979. Red and photographic infrared linear combinations for monitoring vegetation. Remote Sensing of Environment, 8, 127 – 150.

Vermote, E.F., D. Tanre, J.L. Deuze, M. Herman, and J.-J. Morcette. 1997. “Second Simulation of the Satellite Signal in the Solar Spectrum, 6S: An Overview.” *IEEE Transactions on Geoscience and Remote Sensing* 35 (3): 675–86.

Wang, Cuizhen, Jiaguo Qi, and Mark Cochrane. 2005. “Assessment of Tropical Forest Degradation with Canopy Fractional Cover from Landsat ETM+ and IKONOS Imagery.” *Earth Interactions* 9 (22): 1–18.

Werf, G. R. van der, D. C. Morton, R. S. DeFries, J. G. J. Olivier, P. S. Kasibhatla, R. B. Jackson, G. J. Collatz, and J. T. Anderson. 2009. “CO2 Emissions from Forest Loss.” *Nature Geoscience* 2: 737–38.

Williams, Darrel L., Samuel Goward, and Terry Arvidson. 2006. “Landsat: Yesterday, Today, and Tomorrow.” *Photogrammetric Engineering & Remote Sensing* 72 (10): 1171–78.

Woodcock, Curtis E., Richard Allen, Martha Anderson, Alan Belward, Robert Bindschadler, Warren Cohen, Feng Gao, et al. 2008. “Free Access to Landsat Imagery.” *Science* 320 (5879): 1011.

Woodcock, Curtis E., and Alan H. Strahler. 1987. “The Factor of Scale in Remote Sensing.” *Remote Sensing of Environment* 21 (3): 311–32.

Wulder, Michael A., Jeffrey G. Masek, Warren B. Cohen, Thomas R. Loveland, and Curtis E. Woodcock. 2012. “Opening the Archive: How Free Data Has Enabled the Science and Monitoring Promise of Landsat.” *Landsat Legacy Special Issue* 122 (0): 2–10.

Wulder, Michael A, Stephanie M Ortlepp, Joanne C White, and Susan Maxwell. 2008. “Evaluation of Landsat-7 SLC-off Image Products for Forest Change Detection.” *Canadian Journal of Remote Sensing* 34 (2): 93–99.

Xiao, Jingfeng, and Aaron Moody. 2005. “A Comparison of Methods for Estimating Fractional Green Vegetation Cover within a Desert-to-Upland Transition Zone in Central New Mexico, USA.” *Remote Sensing of Environment* 98 (2–3): 237–50.

Zhu, Zhe, and Curtis E. Woodcock. 2012. “Object-Based Cloud and Cloud Shadow Detection in Landsat Imagery.” *Remote Sensing of Environment* 118 (0): 83–94.